

# De-contamination of cosmological 21-cm maps

Liron Gleser<sup>1</sup>, Adi Nusser<sup>1</sup>, Andrew J. Benson<sup>2</sup>

<sup>1</sup>*Physics Department, Technion, Haifa 32000, Israel*

<sup>2</sup>*Theoretical Astrophysics, Caltech, MC130-33, 1200 E. California Blvd, Pasadena, CA 91125, U.S.A.*

27 October 2008

## ABSTRACT

We present a method for extracting the expected cosmological 21-cm signal from the epoch of reionization, taking into account contaminating radiations and random instrumental noise. The method is based on the maximum a-posteriori probability (MAP) formalism and employs the coherence of the contaminating radiation along the line-of-sight and the three-dimensional correlations of the cosmological signal. We test the method using a detailed and comprehensive modeling of the cosmological 21-cm signal and the contaminating radiation. The signal is obtained using a high resolution N-body simulation where the gas is assumed to trace the dark matter and is reionized by stellar radiation computed from semi-analytic galaxy formation recipes. We model contaminations to the cosmological signal from synchrotron and free-free galactic foregrounds and extragalactic sources including active galactic nuclei, radio haloes and relics, synchrotron and free-free emission from star forming galaxies, and free-free emission from dark matter haloes and the intergalactic medium. We provide tests of the reconstruction method for several rms values of instrumental noise from  $\sigma_N = 1$  to 250 mK. For low instrumental noise, the recovered signal, along individual lines-of-sight, fits the true cosmological signal with a mean rms difference of  $d_{\text{rms}} \approx 1.7 \pm 0.6$  for  $\sigma_N = 1$  mK, and  $d_{\text{rms}} \approx 4.2 \pm 0.4$  for  $\sigma_N = 5$  mK. The one-dimensional power spectrum is nicely reconstructed for all values of  $\sigma_N$  considered here, while the reconstruction of the two-dimensional power spectrum and the Minkowski functionals is good only for noise levels of the order of few mK.

**Key words:** cosmology: theory — diffuse radiation — large-scale structure of Universe — intergalactic medium — radio lines: general

## 1 INTRODUCTION

The Wilkinson Microwave Anisotropy Probe (WMAP, Spergel et al. 2007) polarization measurement of the cosmic microwave background (CMB) indicates a value of  $\tau = 0.089 \pm 0.030$  for the optical depth for Thomson scattering with intervening free electrons in the intergalactic medium (IGM). This value for the optical depth implies the presence of ionizing radiation at redshifts  $z > 10$  when the Universe is less than half a Gyr old (see Meiksin 2007 for a review). The ionizing radiation could be of varying nature depending on the type of available sources as a function of time. X-ray radiation emitted from mini black holes (Ricotti & Ostriker 2004) could be responsible for an early stage of (pre)-reionization. Because of their large mean free path for photo-ionization, X-rays tend to maintain the IGM at only partial reionization although full reionization is possible near the sources (Zaroubi et al. 2007; Thomas & Zaroubi 2007). This possible X-ray pre-reionization is followed by UV reionization which begins by the formation of individual H II

bubbles embedded the neutral medium. At a later stage H II bubbles overlap until complete reionization is obtained.

The CMB polarization measurement is proportional to the line-of-sight integral of the ionized fraction and, therefore, is incapable of constraining the details of the reionization process. Absorption features in the spectra of high redshift quasars offer an alternative probe of reionization. However, the dearth of quasars at the relevant redshifts limits the applicability of this probe. Currently, a great deal of effort is being made at observing the 21-cm signal from neutral hydrogen from high redshifts. If the spin temperature of the high redshift H I is different from the CMB then redshifted 21-cm radiation could be detected by radio observations at the relevant frequency range (around 130 MHz for gas at  $z \sim 10$ ). Maps of this cosmological signal constrain the three-dimensional (3D) distribution of H I in the Universe, and, therefore, they could prove to be the most useful probe of reionization. These maps will contain 3D information on the distribution of H I and the ionized fraction as

a function of time. Hopefully, in the near future radio telescopes like the Low Frequency Array (LOFAR),<sup>★</sup> the Precision Array to Probe Epoch of Reionization (PAPER),<sup>†</sup> the Mileura Widefield Array (MWA),<sup>‡</sup> the 21 Centimeter Array (21CMA, formerly PaST),<sup>§</sup> and the Square Kilometer Array (SKA),<sup>¶</sup> will be able to provide such 3D maps.

One of the main obstacles in extracting cosmological information from redshifted 21 cm maps is the subtraction of non-cosmological contaminations due to instrumental noise, ionospheric distortion, galactic and extragalactic foregrounds. In the last few years an effort was made to model the galactic foregrounds (e.g. Jelic et al. 2008; Santos, Cooray & Knox 2005; Wang et al. 2006; Zaldarriaga, Furlanetto & Hernquist 2004), and the extragalactic foregrounds (e.g. Cooray & Furlanetto 2004; Di Matteo et al. 2002; Di Matteo, Ciardi & Miniati 2004; Jelic et al. 2008; Oh & Mack 2003; Santos, Cooray & Knox 2005). In the first part of this work we model the galactic and extragalactic foregrounds and produce 3D maps of the extragalactic foregrounds.

The question of removing the foregrounds has been discussed before. Most of the previous papers have focused on the angular power spectrum of the signal and assumed rather limited spectral resolution (e.g. Di Matteo et al. 2002; Di Matteo, Ciardi & Miniati 2004; Oh & Mack 2003; Santos, Cooray & Knox 2005; Zaldarriaga, Furlanetto & Hernquist 2004; Morales & Hewitt 2004; Morales, Bowman & Hewitt 2006). In general subtraction methods that have been suggested so far includes three stages: bright source removal (e.g. Di Matteo et al. 2002; Di Matteo, Ciardi & Miniati 2004), spectral fitting (Jelic et al. 2008; Zaldarriaga, Furlanetto & Hernquist 2004; Santos, Cooray & Knox 2005; Wang et al. 2006), and residual error subtraction (Morales & Hewitt 2004; Morales, Bowman & Hewitt 2006). Using the fact that the foregrounds which contaminate the 21-cm cosmological signal have much smoother frequency spectra, Wang et al. 2006 developed a method to remove the foregrounds along the line-of-sight. Based on the maximum a-posteriori probability (MAP) formalism we develop a method to reconstruct the 3D maps of the 21-cm cosmological signal from the contaminated noisy data. This method also relies on the smoothness of the contaminating radiation and further assumes a prior for the correlation properties of the cosmological signal. On the other hand, in this method bright sources does not get any special treatment so no empty holes are left in the map. The random noise is also included in the method so there is no need for the three stages framework.

The paper is organized as follows. In § 2, we briefly review the physics behind the 21-cm line. A brief description of the simulation appears in § 3. In § 4 we present our models for the different foregrounds, and in § 5 we describe the method for the cosmological signal reconstruction. We

conclude with a summary and a discussion of the results in § 6.

## 2 THE 21-CM COSMOLOGICAL SIGNAL

The 21-cm line is produced in the transition between the triplet and singlet sub-levels of the hyperfine structure of the ground level of neutral hydrogen atoms. This wavelength corresponds to a frequency of 1420 MHz and a temperature of  $T_* = 0.068$  K. The spin temperature,  $T_s$ , is defined according to the relative population of the triplet,  $n_1$ , to the singlet,  $n_0$ , sub-levels

$$\frac{n_1}{n_0} = 3 \exp\left(-\frac{T_*}{T_s}\right). \quad (1)$$

An H I region would be visible against the CMB either in absorption if  $T_s < T_{\text{CMB}}$  or emission if  $T_s > T_{\text{CMB}}$ , where  $T_{\text{CMB}} \approx 2.73(1+z)$  K is the CMB temperature. There are various mechanisms for raising  $T_s$  significantly above  $T_{\text{CMB}}$  during the epoch of reionization and hence a significant cosmological 21-cm signal is expected.

Intensities,  $I(\nu)$ , at radio frequency are expressed in terms of brightness temperature, defined as  $T_b = I(\nu)c^2/(2k_B\nu^2)$ , where  $c$  is the speed of light and  $k_B$  is Boltzmann's constant. The differential brightness temperature of the 21-cm line emission against the CMB of a small patch of gas at redshift  $z$  is (e.g. Ciardi & Madau 2003)

$$\delta T_b = 16\text{mK } x_{\text{H I}} (1 + \delta) \left(1 - \frac{T_{\text{CMB}}}{T_s}\right) \times \left(\frac{\Omega_b h}{0.02}\right) \left[\left(\frac{1+z}{10}\right) \left(\frac{0.3}{\Omega_m}\right)\right]^{1/2}, \quad (2)$$

where  $x_{\text{H I}}$  is the fraction of H I in the patch, and  $\delta = \rho/\bar{\rho} - 1$  is the density contrast of the gas. In this paper we assume  $T_s \gg T_{\text{CMB}}$  (e.g. Madau, Meiksin & Rees 1997; Nusser 2005a; Chuzhoy & Zheng 2007). In the top panel of Fig. 1 we present a typical cosmological 21-cm signal along one line-of-sight from  $z = 11$  ( $\nu \approx 120$  MHz) to  $z = 7$  ( $\nu \approx 180$  MHz) where the gas in the IGM is completely ionized in our simulation (see § 3). We also calculated the mean differential brightness temperature,  $\langle \delta T_b \rangle$ , for this line-of-sight (dashed line)<sup>||</sup>. In the bottom panel we show the mean ionization fraction,  $f_{\text{ion}}$  of the simulation box. As expected  $\langle \delta T_b \rangle$  decreases as  $f_{\text{ion}}$  increases.

## 3 THE SIMULATION

In order to produce 3D maps of the cosmological 21-cm signal and the foregrounds, we use high resolution N-body simulation where the gas is assumed to trace the dark matter and is reionized by stellar radiation estimated from semi-analytic galaxy formation recipes (Benson et al. 2001 &

<sup>★</sup> <http://www.lofar.org>

<sup>†</sup> <http://astro.berkeley.edu/~dbacker/EoR/>

<sup>‡</sup> <http://www.haystack.mit.edu/ast/arrays/mwa/>

<sup>§</sup> <http://cosmo.bao.ac.cn/project.html>

<sup>¶</sup> <http://www.skatelescope.org>

<sup>||</sup> The fitting formula for the mean differential brightness temperature is  $\delta T_b = \exp[a_0 + a_1 \ln(\nu/\nu_*) + a_2 \ln^2(\nu/\nu_*)]$ , where  $\nu_* = 150$  MHz. The same formula will be use in §5 to fit the foregrounds contamination.

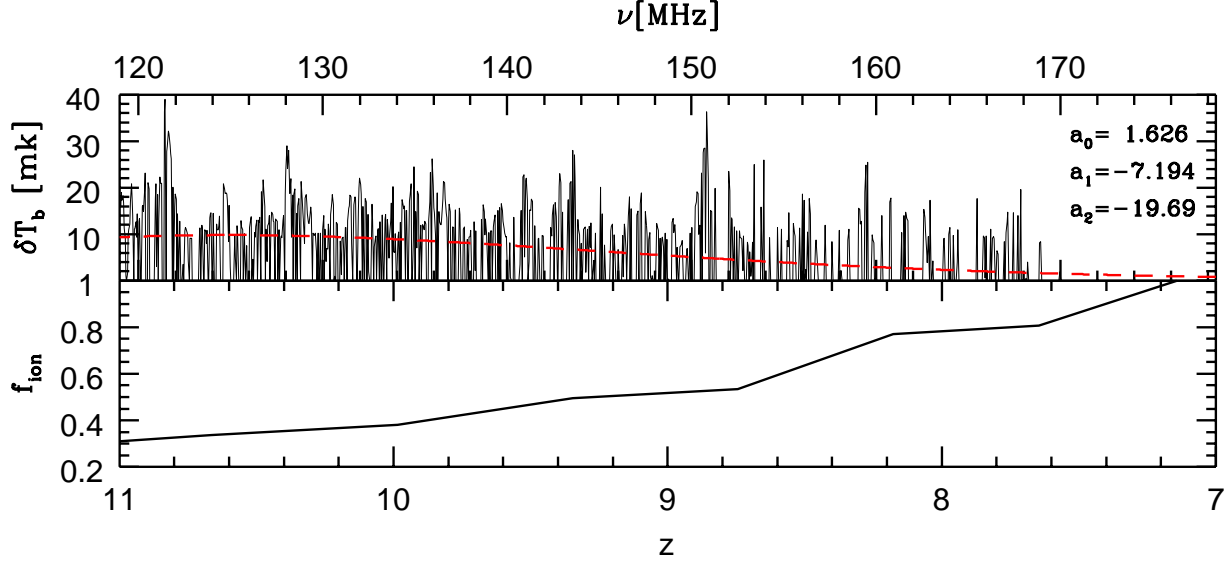


**Figure 1.** Top panel: the cosmological 21-cm signal along a typical line-of-sight from  $z = 11$  ( $\nu \approx 120$  MHz) to  $z = 7$  ( $\nu \approx 180$  MHz). The dashed line shows the fit  $\delta T_b = \exp[a_0 + a_1 \ln(\nu/\nu_*) + a_2 \ln^2(\nu/\nu_*)]$ , where  $\nu_* = 150$  MHz. Bottom panel: The mean ionization fraction in the simulation box as a function of redshift.

2006). We calculate from the simulation the dark matter and gas number density, the mass and number of dark matter haloes, and the gas ionization fraction, all as a function of redshift.

The simulation box size is  $141.3 \text{ h}^{-1}\text{Mpc}$  comoving and it contains  $256^3$  particles, where each particle mass is  $M_p = 2 \times 10^{10} M_\odot$ . We use a  $\Lambda$ CDM cosmology with  $\Omega_m = 0.3$ ,  $\Omega_\Lambda = 0.7$ ,  $h = 0.7$ , and  $\sigma_8 = 0.9$ . The galaxy formation model includes Compton cooling,  $\text{H}_2$  cooling and weak feedback from supernova explosions, and the ionizing photons escape fraction from galaxies is 0.15 (Benson et al. 2006). The reader is referred to that paper, and references therein, for a full description of the simulation.

#### 4 FOREGROUNDS

The 21-cm cosmological signal will suffer from several sources of contamination. Here we focus on the contamination which is produced by foreground radiation emitted from galactic and extragalactic sources and add a random instrumental noise with a rms value  $\sigma_N$ . We have assumed that the necessary correction of ionospheric distortion, by means of radio adaptive optics, and the calibration of the time-variable gain, phase, and polarization of each antenna of the radio telescope array, were already taking care of. Although the contaminating radiation could be as much as  $10^5$  times larger than the cosmological signal (e.g. Gnedin & Shaver 2004; McQuinn et al. 2006; Morales, Bowman & Hewitt 2006), their typical power-law dependence on frequency should allow us to disentangle the small scale variations of the cosmological signal. In the following we describe our modeling of the foreground contaminations.

Two physical processes are responsible for most con-

taminations: synchrotron radiation and free-free emission. Synchrotron radiation arises from acceleration of relativistic electrons in magnetic fields. Assuming a power-law dependence of the electron number density on energy,  $N(E) \sim E^{-\gamma}$ , where  $E$  is the electron energy, one obtains a synchrotron flux  $I_{\text{syn}} \sim \nu^{-\alpha}$  with spectral index  $\alpha = (\gamma - 1)/2$ . The corresponding brightness temperature is  $T_b \propto I_{\text{syn}}(\nu)\nu^{-2} \propto \nu^{-\beta}$ , where  $\beta = \alpha + 2$ . We will consider synchrotron radiation from our Galaxy, star forming galaxies, radio galaxies and radio haloes and relics in clusters. For each of these systems we will assume a power-law synchrotron emissivity consistent with the respective observational constraints (see below).

The emissivity of the free-free radiation from diffuse ionized gas is (Rybicki & Lightman 1979):

$$\epsilon_\nu(n_e, T_e) = 5.4 \times 10^{-39} n_e^2 T_e^{-1/2} g_{\text{ff}}(\nu, T_e) \times e^{-h\nu/k_B T_e} \text{ erg cm}^{-3} \text{ s}^{-1} \text{ Hz}^{-1} \text{ sr}^{-1}, \quad (3)$$

where the Gaunt factor is approximately  $g_{\text{ff}}(\nu, T_e) \approx 11.96 T_e^{0.15} \nu^{-0.1}$  in the radio regime (Lang 1999),  $n_e$  and  $T_e$  are the electron number density and temperature, and  $\nu = \nu_{\text{obs}}(1 + z)$  is the emitted frequency, with  $\nu_{\text{obs}}$  the observed frequency. Therefore, the free-free flux density also has a power-law dependence on frequency with spectral index  $\alpha = 0.1$  ( $\beta = 2.1$ ).

##### 4.1 Galactic foregrounds

The galactic foregrounds are generated by synchrotron, free-free, thermal and spinning dust emissions. In the relevant frequency range, between  $\sim 100$  and  $\sim 200$  MHz, galactic synchrotron emission is the most dominant foreground, responsible for  $\sim 98.5\%$  of the total galactic contamination, free-free

emission from the diffuse ionized hydrogen in the interstellar medium (ISM) contributes  $\sim 1.5\%$  (Shaver et al. 1999), and dust emission is negligible (Platania et al. 2003; Reich, Testori & Reich 2001). One should also take into account radio recombination lines from our Galaxy. Since these lines occur at specific frequencies, template spectra can be used to remove them, without previous knowledge of their actual intensity (e.g. Morales, Bowman & Hewitt 2006).

The synchrotron emission process is probably due to radiation from high energy cosmic-ray electrons above a few MeV in the galactic magnetic field (e.g. Pacholczyk 1970; Banday & Wolfendale 1990, 1991). There is less contamination in relatively smooth regions away from the galactic plane and galactic loops. Following Wang et al. (2006) we assume a running power-law in frequency for the galactic synchrotron brightness temperature,

$$T_{\text{syn}} = A_{\text{syn}} \left( \frac{\nu}{\nu_*} \right)^{-\beta_{\text{syn}} - \Delta\beta_{\text{syn}} \log(\nu/\nu_*)}, \quad (4)$$

where  $A_{\text{syn}}$  is synchrotron brightness temperature at  $\nu_* = 150$  MHz, and  $\beta_{\text{syn}}$  and  $\Delta\beta_{\text{syn}}$  are the spectral index and spectral running index, respectively. Using the 408 MHz all-sky continuum survey of Haslam et al. (1981, 1982), Haverkorn, Katgert & de Bruyn (2003) estimated the mean brightness temperature at 408 MHz to be  $\sim 33$  K with temperature uncertainty of  $\sim 10\%$ . After subtraction of the  $\sim 2.7$  K contribution of the CMB and the  $\sim 3.1$  K contribution of extragalactic sources (e.g. Bridle 1967; Lawson et al. 1987; Reich & Reich 1988), the diffuse synchrotron galactic background is  $\sim 27.2$  K. Assuming a spectral index of 2.74 (Platania et al. 2003) we estimate the synchrotron brightness temperature at 150 MHz to be  $A_{\text{syn}} = 442.0 \pm 44.2$  K. At high galactic latitudes, the brightness temperature can drop to minimum of  $\sim 200$  K (Lawson et al. 1987; Reich & Reich 1988; Shaver et al. 1999). The estimations for the mean spectral index around 150 MHz are ranged from 2.6 to 2.8 (e.g. Bridle 1967; Willis et al. 1977; Lawson et al. 1987; Reich & Reich 1988; Banday & Wolfendale 1990, 1991; Tegmark et al. 2000; Platania et al. 2003) with indications for dispersion at each position on the sky, due to distinct components along the line-of-sight (e.g. Lawson et al. 1987; Reich & Reich 1988; Banday & Wolfendale 1990, 1991; Shaver et al. 1999). We choose spectral index of  $\beta_{\text{syn}} = 2.7$  with dispersion of 0.1 (Reich & Reich 1988; Shaver et al. 1999), and spectral running index of  $\Delta\beta_{\text{syn}} = 0.1$  (Tegmark et al. 2000; Wang et al. 2006).

Free-free thermal emission appears in ionized regions in the ISM, with electron temperature of  $T_e > 8000$  K. As for the galactic synchrotron, we assume a running power-law in frequency for the galactic free-free brightness temperature (Wang et al. 2006),

$$T_{\text{ff}} = A_{\text{ff}} \left( \frac{\nu}{\nu_*} \right)^{-\beta_{\text{ff}} - \Delta\beta_{\text{ff}} \log(\nu/\nu_*)}, \quad (5)$$

where  $A_{\text{ff}}$  is the free-free brightness temperature at  $\nu_* = 150$  MHz, and  $\beta_{\text{ff}}$  and  $\Delta\beta_{\text{ff}}$  are the spectral index and spectral running index, respectively. Maintaining the 70:1 ratio between the synchrotron and free-free emission (Shaver et al. 1999), we adopted  $A_{\text{ff}} = 6.33 \pm 0.63$  K assuming 10% temperature uncertainty. At high frequencies ( $\nu > 10$  GHz) the brightness temperature spectral index is  $\beta_{\text{ff}} = 2.15$ , while at

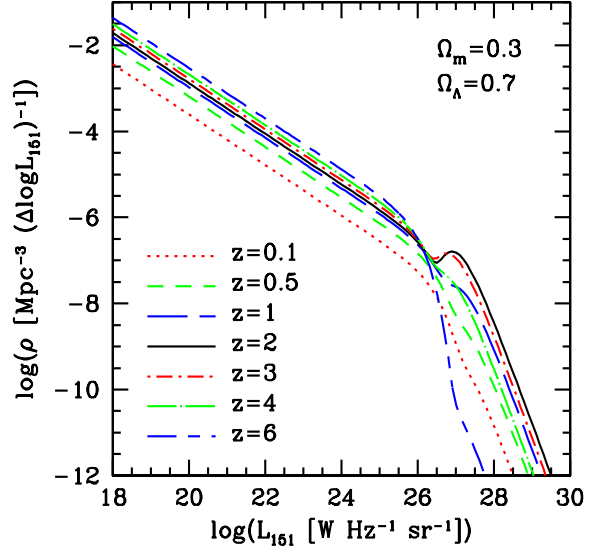


**Figure 2.** The Willott et al. (2001) RLF (model C) for  $\Lambda$ CDM cosmology at seven redshifts from  $z = 0.1$  to  $z = 6$ .

low frequencies it drops to  $\beta_{\text{ff}} = 2.0$  due to optically thick self-absorption (Bennett et al. 2003). Since the gas is optically thin above few MHz, the brightness temperature spectrum between  $\sim 100$  and  $\sim 200$  MHz is well determined with a spectral index of  $\beta_{\text{ff}} = 2.10 \pm 0.01$  (Shaver et al. 1999), and the spectral running index is  $\Delta\beta_{\text{ff}} = 0.01$  (Tegmark et al. 2000; Wang et al. 2006).

## 4.2 Extragalactic foregrounds

The total emission of extragalactic foregrounds has been estimated both directly and from integrated source counts. At 150 MHz, its contribution to the contamination varies from  $\sim 30$  K (Willis et al. 1977; Cane 1979) to  $\sim 50$  K (Bridle 1967; Lawson et al. 1987; Reich & Reich 1988). These foregrounds produce  $\sim 10\%$  of the total contamination on average, but can reach  $\sim 25\%$  at high galactic latitudes, where the minimum brightness temperature of the diffuse galactic emission drops to  $\sim 200$  K (Lawson et al. 1987; Reich & Reich 1988; Shaver et al. 1999).

Most foregrounds are due to radio point sources and relate to active galactic nuclei (AGN) activity. Radio haloes and radio relics are also significant foregrounds, but since they appear only in rich galaxy clusters, they are rare. The remaining extragalactic foregrounds, which are also the less significant ones, are synchrotron and free-free emission from star forming galaxies, and free-free emission from ionized hydrogen dark matter haloes and diffuse IGM.

### 4.2.1 Radio emission from AGNs

Radio emission from AGNs is linked to the accretion of gas on massive black holes at the centers of galaxies. In order to

incorporate this contamination in the simulation we determine the number of AGNs in the simulation box according to the radio luminosity function (RLF), and assume that the AGN distribution follows the underlying mass density field. The RLF is defined as the number of radio galaxies and quasars per comoving volume per unit (base 10) logarithm of luminosity,  $\rho(L, z)$ , where  $L$  is the radio luminosity derived from the flux-density  $S$  and redshift per frequency and steradians.

We use the RLF model of Willott et al. (2001) to calculate the background flux density from AGNs, assuming the luminosity of an AGN has a power-law dependence on frequency with a spectral index of  $0.80 \pm 0.15$ . They used three redshift surveys of flux-limited samples selected at the radio frequency range of our interest: 7CRS (at 151 MHz with flux density  $S_{151} \geq 0.5$  Jy), 3CRR (at 178 MHz with  $S_{178} \geq 10.9$  Jy), and 6CE (at 151 MHz with  $2.0 \geq S_{151} < 3.93$  Jy).

Willott et al. (2001) separated the radio sources to low- and high-luminosity populations. A combination of the low-luminosity RLF,  $\rho_l$ , and the high-luminosity RLF,  $\rho_h$ , gives the total RLF

$$\rho(L, z) = \rho_l + \rho_h. \quad (6)$$

They checked three models for the redshift distribution. In our work we use their redshift distribution which has a one-tailed Gaussian rise to the peak redshift and then a one-tailed Gaussian decline at higher redshifts (model C) with  $\Omega_m = \Omega_\Lambda = 0$  cosmology (for more details see §3 in their paper).

The low-luminosity RLF is

$$\rho_l = \begin{cases} \rho_{l0} \left( \frac{L}{L_{l*}} \right)^{-\alpha_l} \exp \left( \frac{-L}{L_{l*}} \right) (1+z)^{k_l} & z < z_{l0} \\ \rho_{l0} \left( \frac{L}{L_{l*}} \right)^{-\alpha_l} \exp \left( \frac{-L}{L_{l*}} \right) (1+z_{l0})^{k_l} & z \geq z_{l0} \end{cases}, \quad (7)$$

where  $\log(\rho_{l0}) = -7.523$ ,  $\log(L_{l*}) = 26.48$ ,  $\alpha_l = 0.586$ ,  $k_l = 3.48$ , and  $z_{l0} = 0.710$ .

The high-luminosity RLF is

$$\rho_h = \rho_{h0} \left( \frac{L}{L_{h*}} \right)^{-\alpha_h} \exp \left( -\frac{L}{L_{h*}} \right) f_h(z), \quad (8)$$

where  $\log(\rho_{h0}) = -6.757$ ,  $\log(L_{h*}) = 27.39$ ,  $\alpha_h = 2.42$ , and the high-luminosity evolution function  $f_h(z)$  is

$$f_h(z) = \exp \left[ -\frac{1}{2} \left( \frac{z - z_{h0}}{z_{h1}} \right)^2 \right] \quad (9)$$

for  $z < z_{h0}$ , and

$$f_h(z) = \exp \left[ -\frac{1}{2} \left( \frac{z - z_{h0}}{z_{h2}} \right)^2 \right] \quad (10)$$

for  $z \geq z_{h0}$ , where  $z_{h0} = 2.03$ ,  $z_{h1} = 0.568$ , and  $z_{h2} = 0.956$ .

To convert the RLF with  $\Omega_m = \Omega_\Lambda = 0$  cosmology,  $\rho_0$ , to RLF of  $\Lambda$ CDM cosmology,  $\rho_{\Lambda\text{CDM}}$ , we used the following relation from Peacock (1985)

$$\rho_{\Lambda\text{CDM}}(L_{\Lambda\text{CDM}}, z) \frac{dV_{\Lambda\text{CDM}}}{dz} = \rho_0(L_0, z) \frac{dV_0}{dz}, \quad (11)$$

where  $V_{\Lambda\text{CDM}}$  and  $V_0$  are the comoving volume in  $\Lambda$ CDM and  $\Omega_m = \Omega_\Lambda = 0$  cosmologies, respectively. The relation

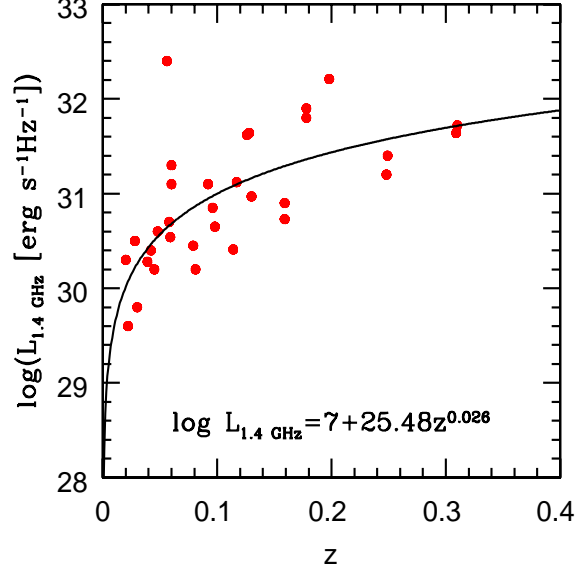


**Figure 3.** The relic radio luminosity at 1.4 GHz as a function of the cluster redshift, where the full circles are the data from Giovannini & Feretti (2004), and the solid line is our model best fit.

between the luminosities  $L_{\Lambda\text{CDM}}$  and  $L_0$  is  $L_{\Lambda\text{CDM}}/L_0 = (D_{\Lambda\text{CDM}}/D_0)^2$ , where  $D_{\Lambda\text{CDM}}$  and  $D_0$  are the corresponding distances in the two cosmologies (see Peacock 1985; Dunlop & Peacock 1990 for more details). In Fig. 2 we present the RLF for  $\Lambda$ CDM cosmology at six redshifts, from 0.1 to 6.

#### 4.2.2 Radio haloes & relics

Diffuse non-thermal radio emission from the intra-cluster medium (ICM) is observed in about 30 percent of rich galaxy clusters, which can be found in dark matter haloes with  $M_{\text{halo}} \gtrsim 5 \times 10^{14} M_\odot$ . These sources are classified as *radio haloes* when their morphology is regular, centered on and resembling the X-ray emissivity, or *radio relics* when they are irregular, of elongated shapes, and located at the periphery of the cluster (e.g. Giovannini & Feretti 2004). For weak magnetic fields ( $B < 0.5 \mu\text{G}$ ), the inverse Compton losses are dominant, while for stronger magnetic fields, synchrotron emission is dominant (e.g. Cassano et al. 2006).

Cassano et al. (2006) studied the statistics of giant radio haloes (GRHs) from electron re-acceleration models. We use this study to determine the probability that a halo in the simulation hosts a GRH of a given radio emissivity, as function of the halo mass and redshift (see their Fig. 17a). The radio halo luminosity at 1.4 GHz is

$$L_{1.4 \text{ GHz}} = (4.85 \pm 1.64) \times 10^{30} \left( \frac{M_{\text{vir}}}{10^{15} M_\odot} \right)^{\alpha_M} \text{erg s}^{-1} \text{Hz}^{-1}, \quad (12)$$

where  $M_{\text{vir}}$  is the virial mass of the halo in  $M_\odot$ , and  $\alpha_M = 2.9 \pm 0.4$ . The radio halo luminosity per steradian

**Table 1.** The relevant components of the ISM: the warm neutral medium (WNM), the warm ionized medium (WIM), and the hot ionized medium (HIM), neglecting the molecular medium (MM) and the cold neutral medium (CNM) which are completely neutral and occupy less than 2% of the galaxy volume.  $T_e$  is the gas temperature,  $n_H$  is the hydrogen number density,  $x_e = n_e/n_H$  is the ionization fraction.  $f_V$  is the fraction of the interstellar volume, and  $|Z|$  is the extent of the gas component normal to the disk plane. The following values are based on data from Heiles (2001) and Tüllmann (2002).

	$T_e$ [ $10^4$ K]	$n_H$ [ $\text{cm}^{-3}$ ]	$x_e$	$f_V$	$ Z $ extent [kpc]
WNM	0.05-0.8	0.1-0.5	0.2	0.4	0.5
WIM	0.8-1	0.05-0.08	1	0.1	5
HIM	10-1000	0.003-0.006	1	0.5	7

at frequency  $\nu$  is

$$L_{\text{GRH}}(\nu) = \frac{L_{1.4 \text{ GHz}}}{4\pi} \left( \frac{\nu}{1.4 \text{ GHz}} \right)^{-\alpha_\nu} \text{erg Mpc}^{-3} \text{s}^{-1} \text{Hz}^{-1} \text{sr}^{-1}, \quad (13)$$

where  $\alpha_\nu = 1.2$  (Cassano et al. 2006).

Radio relics are probably related to shock waves generated by cluster mergers. These shock fronts can revive old radio ghosts when the thermal pressure is much higher than the magnetic field pressure (Enßlin & Gopal-Krishna 2001; Hoeft et al. 2004). Since the available data and knowledge on radio relics are still poor, there is no statistical model for the occurrence probability and radio luminosity of relics as a function of the halo mass and redshift. Therefore, we assume a 30% probability for a radio relic to exist in massive dark matter haloes,  $M_{\text{halo}} \gtrsim 5 \times 10^{14} M_\odot$  (e.g. Di Matteo, Ciardi & Miniati 2004). Giovannini & Feretti (2004) presented data from about 30 clusters of galaxies where at least one radio relic is present. We use these data to roughly estimate the relic radio luminosity at 1.4 GHz in  $\text{erg s}^{-1} \text{Hz}^{-1}$  as a function of the cluster redshift  $z$  (see Fig 3)

$$\log L_{1.4 \text{ GHz}} = 7 + (25.48 \pm 0.27) z^{0.026 \pm 0.004} \text{erg s}^{-1} \text{Hz}^{-1}. \quad (14)$$

The radio relic luminosity per steradians at frequency  $\nu$  is

$$L_{\text{RLC}}(\nu) = \frac{L_{1.4 \text{ GHz}}}{4\pi} \left( \frac{\nu}{1.4 \text{ GHz}} \right)^{-\alpha_\nu} \text{erg s}^{-1} \text{Hz}^{-1} \text{sr}^{-1}, \quad (15)$$

where  $\alpha_\nu = 1.2$  (Kempner et al. 2004).

#### 4.2.3 Star forming galaxies

The gas in the ISM of star forming galaxies is mainly heated and ionized by supernovae explosions, stellar winds and cosmic rays. We calculated the free-free emission from the ISM components with a significant ionized fraction: the warm neutral medium (WNM), the warm ionized medium (WIM), and the hot ionized medium (HIM). While neglecting the molecular medium (MM) and the cold neutral medium (CNM) which are completely neutral and occupy less than 2% of the galaxy volume (e.g. Heiles 2001; Tüllmann 2002).

In table 1 we present the physical properties of the relevant ISM components for free-free emission. We used these data and the free-free emissivity from equation (3) to calculate the luminosity of an ISM component  $i$  of a single star forming galaxy

$$L_\nu^i(z) \approx \epsilon_\nu(n_e^i, T_e^i) V_{\text{ion}}^i(z) \text{erg s}^{-1} \text{Hz}^{-1} \text{sr}^{-1}, \quad (16)$$

where  $n_e^i = n_H^i x_e^i$  is the free electrons number density of the component,  $T_e^i$  is the component temperature, and  $V_{\text{ion}}^i \approx 2\pi f_V r^2(z) Z(z)$  is the component ionized volume, where  $r(z)$  is the galaxy radius,  $Z(z) \approx |Z|[r(z)/r_0]$  is the extent height of the galaxy, and  $r_0 = 15$  kpc is the approximate radius of the outer stellar ring of the Milky Way (e.g. Helmi et al. 2003; Ibata et al. 2003; Yanny et al. 2003).

We adopt the Shen et al. (2003) galaxy radius distribution to draw random radii in the simulation. Shen et al. (2003) used a complete set of about 140000 galaxies from the Sloan Digital Sky Survey (SDSS) to study the size distribution of galaxies as a function of magnitude. They assume a log-normal distribution for the galaxy radius

$$f(r, \bar{r}, \sigma_{\ln r}) = \frac{1}{\sqrt{2\pi}\sigma_{\ln r}} \exp \left[ -\frac{\ln^2(r/\bar{r})}{2\sigma_{\ln r}^2} \right] \frac{dr}{r}, \quad (17)$$

where the median,  $\bar{r}(M)$ , and the dispersion,  $\sigma_{\ln r}(M)$ , are functions of the  $r$ -band Petrosian absolute magnitude,  $M$ , in the range  $-24 \lesssim M \lesssim -16$ . For late-type galaxies

$$\bar{r}(M) = [1 + 10^{-0.4(M-M_0)}]^{-\beta-\alpha} 10^{\gamma-0.4\alpha M} \text{kpc}, \quad (18)$$

and

$$\sigma_{\ln r}(M) = \sigma_2 + \frac{\sigma_1 - \sigma_2}{1 + 10^{-0.8(M-M_0)}}, \quad (19)$$

where  $\alpha = 0.26$ ,  $\beta = 0.51$ ,  $\gamma = -1.71$ ,  $\sigma_1 = 0.45$ ,  $\sigma_2 = 0.27$ , and  $M_0 = -20.91$  are fitting parameters. Following Blanton et al. (2001, 2003), we approximate the galaxy luminosity function in the  $r$ -band per unit magnitude by a Schechter function

$$\Phi(M) dM = 0.4 \ln(10) \phi_* 10^{-0.4(M-M_*)} (\alpha+1) \times \exp[-10^{-0.4(M-M_*)}] dM, \quad (20)$$

where at redshift  $z = 0.1$  the fitting parameters are  $\phi_* = 0.0149 \pm 0.0004 \text{ h}^3 \text{Mpc}^{-3}$ ,  $M_* - 5 \log_{10} h = -20.44 \pm 0.01$ , and  $\alpha = -1.05 \pm 0.01$ . We scale the galaxy radii with redshift by  $r(z) \propto H(z)^{-1}$  (Ferguson et al. 2004).

In order to incorporate this contamination in the simulation we determine the galaxy number counts for normal spiral galaxies using the X-ray luminosity function from Ranalli et al. (2005), which based on Takeuchi et al. (2003, 2004) far-infrared (FIR) luminosity function:

$$\varphi(L) = \varphi^* \left( \frac{L}{L^*} \right)^{1-\alpha} \exp \left[ -\frac{1}{2\sigma^2} \log_{10}^2 \left( 1 + \frac{L}{L^*} \right) \right] \quad (21)$$

with  $\varphi^* = 0.0234 \pm 0.0030 \text{ h}^3 \text{Mpc}^{-3}$ ,  $\alpha = 1.23 \pm 0.04$ ,  $\sigma = 0.724 \pm 0.01$ , and  $L^* = (4.4 \pm 0.9) \times 10^8 \text{ h}^{-2} L_\odot$ . The galaxy number counts per comoving volume at redshift  $z$  is

$$N(z) = \int_{L_{\min}(z)}^{L_{\max}(z)} d \log L \varphi(\log L) \text{h}^3 \text{Mpc}^{-3} \quad (22)$$

where the minimum and maximum luminosities at  $z = 0$  are  $L_{\min} = 10^{39} \text{ erg s}^{-1}$  and  $L_{\max} = 10^{43} \text{ erg s}^{-1}$ , respectively.

We consider luminosity evolution of  $L \propto (1+z)^{2.7}$  (Norman et al. 2004; Ranalli et al. 2005). We further assume that the galaxy distribution follows the underlying mass density field.

We use the calculation for free-free emission from star forming galaxies to estimate their synchrotron emission. Shaver et al. (1999) determine a  $\sim 70:1$  ratio between galactic synchrotron and free-free emission at 150 MHz. Therefore, we assume that the synchrotron emission is  $70 \pm 10$  times greater than the free-free emission at 150 MHz. The spectral index of the synchrotron emission depends on the relativistic electrons density distribution which varies from galaxy to galaxy and within each galaxy. Hummel (1991) analyzed the low frequency radio continuum data from 27 spiral galaxies with different galaxy inclinations. He found that the mean synchrotron spectral index of a galaxy at low frequencies ( $\nu \leq 700$  MHz) varies from  $\sim 0.2$  to  $\sim 0.9$  with a mean value of  $\alpha = 0.56 \pm 0.15$ . Since our frequency range of interest is limited to the vicinity of 150 MHz (100-200 MHz), we simplify the frequency dependence by using a mean spectral index of  $\alpha = 0.6$  for all galaxies.

#### 4.2.4 Free-free emission from haloes and IGM

The free-free emission from haloes comes from ionized gas which is confined to dark matter haloes, at the virial temperature. Photo-ionized diffuse gas in the IGM, typically, has a mean temperature of  $10^4$  K. Therefore, only haloes with  $T_{\text{vir}} \geq 10^4$  K are able to confine gas to their gravitational potential well. The virial temperature of a halo of mass  $M_{\text{halo}}$  is given by

$$T_{\text{vir}} = 3.6 \times 10^5 \left( \frac{V_c}{100 \text{ km s}^{-1}} \right)^2 \text{ K}, \quad (23)$$

where the halo circular velocity is

$$V_c = [100 \Omega_m(z) H^2(z) (G M_{\text{halo}})^2]^{1/3}. \quad (24)$$

Neglecting temperature variations across the halo, according to equation (3), the total free-free emissivity of the halo gas is proportional to the spatial integral of  $n_e^2$ . Assuming further that the gas density follows that of the dark matter, the total emissivity becomes proportional to the variance of mass density fluctuations in the halo. To determine the density variance of a halo of mass,  $M_{\text{halo}}$ , at redshift  $z$ , we use the improved halo density profile from Navarro et al. (2004), which is based on the Navarro, Frenk & White (1996, 1997, hereafter NFW) density profile

$$\frac{\rho(r)}{\rho_{-2}} = \exp \left\{ -\frac{2}{\alpha} \left[ \left( \frac{r}{r_{-2}} \right)^\alpha - 1 \right] \right\}, \quad (25)$$

where  $r_{-2} = r_{\text{vir}}/c$  is the characteristic radius in which the NFW density profile is proportional to  $r^{-2}$ ,  $r_{\text{vir}}$  is the virial radius of the halo, and  $c$  is the concentration parameter. To calculate the concentration for arbitrary virial mass and redshift, we used the Eke et al. (2001) code available at J. F. Navarro's home page<sup>\*\*</sup>. The density at  $r_{-2}$  is related to

the NFW characteristic density,  $\rho_s$ , by  $\rho_{-2} = \rho_s/4$ , where

$$\rho_s = \frac{200 \rho_{\text{crit}} c^3}{3 [\ln(1+c) - c/(1+c)]}, \quad (26)$$

where

$$\rho_{\text{crit}}(z) = \frac{3H_0^2}{8\pi G} \frac{\Omega_0}{\Omega(z)} (1+z)^3, \quad (27)$$

where  $H_0$  is the current value of Hubble's constant, and the halo mean density is  $200\rho_{\text{crit}}$ . Following Navarro et al. (2004) we choose  $\alpha = 0.17$ . The mass density variance is

$$\rho_{\text{var}}^2 = \frac{4\pi}{V_{\text{vir}}} \rho_{-2}^2 \int_0^{r_{\text{vir}}} \exp \left\{ -\frac{4}{\alpha} \left[ \left( \frac{r}{r_{-2}} \right)^\alpha - 1 \right] \right\} r^2 dr, \quad (28)$$

where  $V_{\text{vir}} = (4\pi/3)r_{\text{vir}}^3$  is the halo's virial volume. At redshift  $z = 0$ ,  $\rho_{\text{var}}^2/\rho_{\text{crit}}^2 \approx 10^8$  for  $M_{\text{halo}} = 10^8 M_\odot$ , and  $\rho_{\text{var}}^2/\rho_{\text{crit}}^2 \approx 0.5 \times 10^8$  for  $M_{\text{halo}} = 10^{12} M_\odot$ .

We apply the friends-of-friends (FoF) algorithm to identify haloes in the simulation box. Demanding haloes to have 10 particles or more, gives a mass threshold of  $M_{\text{halo}} \geq 2 \times 10^{11} M_\odot$  for haloes in the simulation. Haloes with lower masses are introduced in the simulation according to the Sheth & Tormen (1999) mass function. These haloes are placed at the positions of simulation particles not belonging to haloes identified by the FoF algorithm. We calculate the amount of radiation emanating from each cell in the simulation box by collecting the radiation from all the haloes with virial temperatures,  $T_{\text{vir}} \geq 10^4$  K.

The fraction of diffuse ionized gas in the IGM is taken to equal the fraction of mass in haloes with  $T_{\text{vir}} < 10^4$  K. The free-free emission from diffuse ionized gas in the IGM has a small contribution to the overall contamination. The cumulative specific intensity for the diffuse free-free emission from the IGM is

$$I_\nu = \int d\chi \frac{\epsilon_\nu(n_e, T_e)}{(1+z)^4} \text{ erg cm}^{-2} \text{ s}^{-1} \text{ Hz}^{-1}, \quad (29)$$

where  $d\chi = ca^{-1}dt(z)$  is the differential conformal distance and  $\epsilon_\nu(n_e, T_e)$  is the free-free emissivity from equation (3).

### 4.3 Results

We have implemented the recipes for the foreground contaminations in the simulation box. We work with 65536 lines-of-sight in a square window of  $141.3 \text{ h}^{-1} \text{ Mpc}$  (comoving) on the side and calculate the foregrounds' total intensity in the frequency range  $\nu = 80 - 240$  MHz, corresponding to the 21-cm signal at redshifts  $z \approx 5 - 17$ . In Fig. 4 we show the mean brightness temperature of the various foregrounds. As expected the most significant contamination is the galactic synchrotron foreground ( $\sim 89.5\%$ ), next is the AGN radio emission ( $\sim 8.4 - 9.4\%$ ), and then the galactic free-free ( $\sim 0.9 - 1.8\%$ ). The rest of the extragalactic foregrounds contribute on average  $\sim 0.15\%$ . We also tried several cases

tions for haloes of arbitrary mass and redshift can be found at J. F. Navarro's home page: <http://www.astro.uvic.ca/~jfn/mywebpage/home.html>

<sup>\*\*</sup> A link to the ENS subroutines for calculation of concentra-



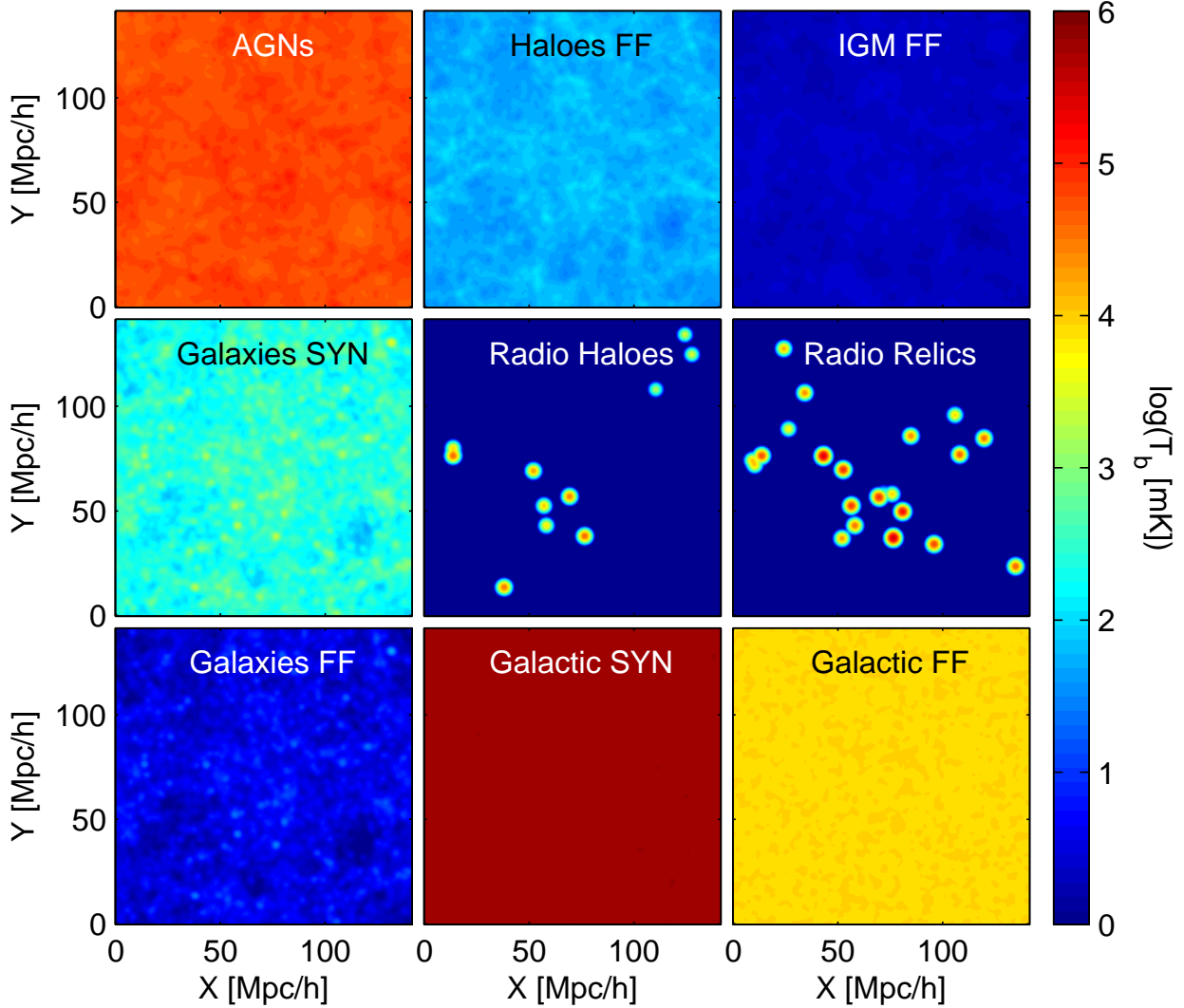


**Figure 5.** Maps of the brightness temperature foregrounds at  $\nu = 129.78$  MHz: radio emission from AGNs (top-left), free-free from haloes (top-middle), free-free from diffuse IGM (top-right), synchrotron from star forming galaxies (center-left), emission from radio haloes (center-middle) and radio relics (center-right), free-free from star forming galaxies (bottom-left), galactic synchrotron (bottom-middle), and galactic free-free (bottom-right).

where we changed the value of the galactic synchrotron emission from a fairly low galactic foreground, which resemble high latitude regions (Shaver et al. 1999), where the contribution of the galactic synchrotron emission drops to  $\sim 77\%$  of the total contamination ( $A_{\text{syn}} = 150 \pm 15$  K) and the galactic free-free emission adds  $\sim 1\%$  ( $A_{\text{ff}} = 2.250 \pm 0.225$  K), to an extremely high galactic foreground, which might be found in radio loops (Reich & Reich 1988), where the galactic synchrotron emission contributes  $\sim 98\%$  of the total contamination ( $A_{\text{syn}} = 2000 \pm 200$  K) and the galactic free-free adds  $\sim 0.4\%$  ( $A_{\text{ff}} = 6.33 \pm 0.63$  K).

In Fig. 5 we present logarithmic maps of the brightness temperature of the integrated extragalactic foregrounds along the lines-of-sight which contaminate the cosmological 21-cm signal at  $z = 10$  ( $\nu = 129.78$  MHz). In Fig. 6 we present the same logarithmic maps but for the brightness temperature contrast,  $\log(T_b / \langle T_b \rangle)$ , where  $\langle T_b \rangle$  is the mean

brightness temperature in each panel. As expected the most dominant foreground is the galactic synchrotron (bottom-middle) and next is the radio emission from AGN (top-left). The free-free emissions from the IGM (top-right), haloes (top-middle) and star forming galaxies (bottom-left) contribute very little to the contamination. The emission from radio haloes (center-middle) and relics (center-right), which seems to be insignificant on average, can actually contribute significant contamination in individual lines-of-sight. Since there are only a few haloes with  $M_{\text{halo}} \gtrsim 5 \times 10^{14} M_{\odot}$  in the simulation box, for most lines-of-sight the contamination is practically zero, while in a few lines-of-sight the brightness temperature contamination from radio halo or relic can be as high as few  $10^5$  mK.



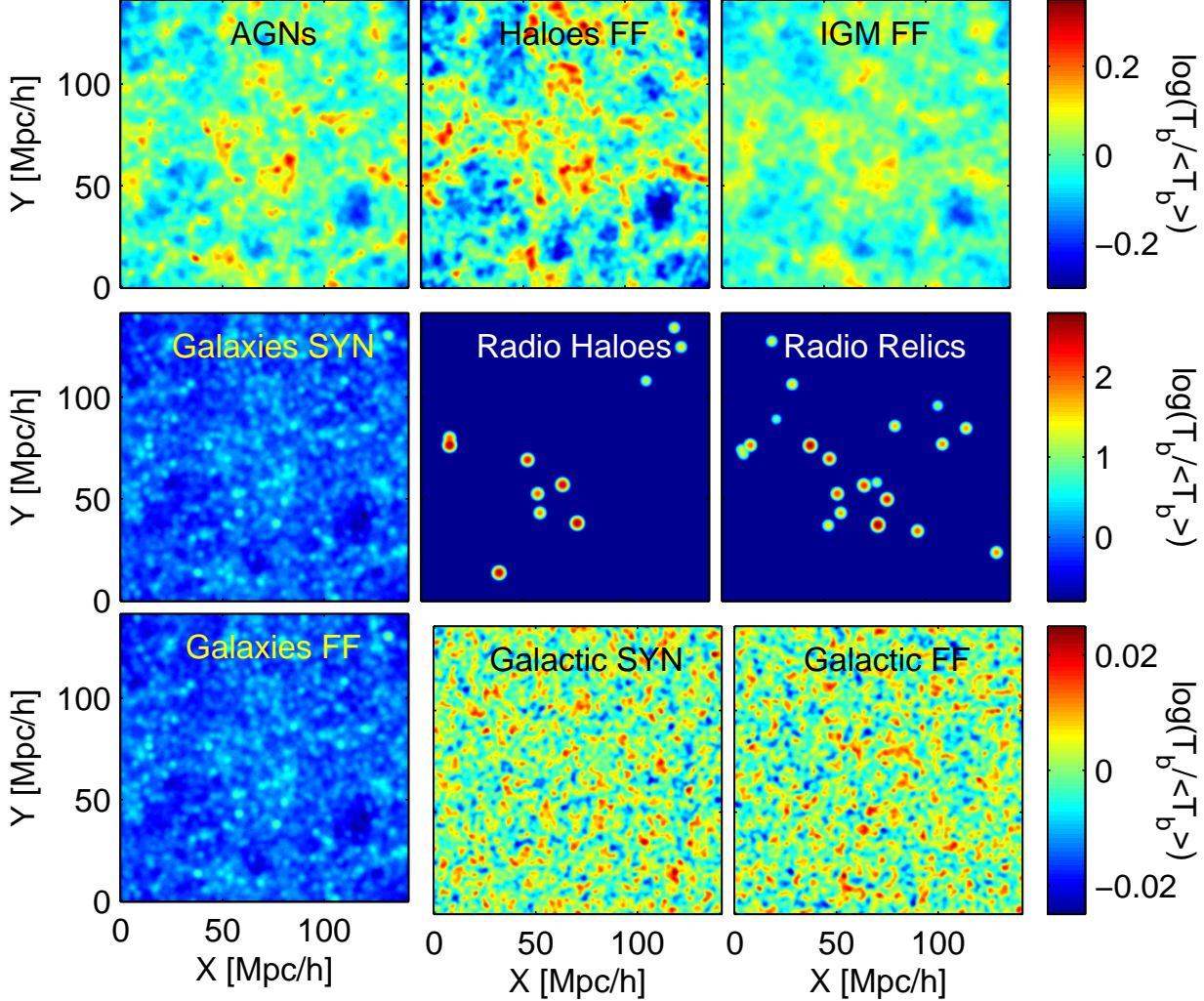


**Figure 6.** The same as Fig. 5, but for the brightness temperature contrast in logarithmic scale,  $\log(T_b/\langle T_b \rangle)$ , where  $\langle T_b \rangle$  is the mean brightness temperature in each panel. The three top panels are scaled from -0.3 to 0.35. The three central panels and the bottom-left panel are scaled from -0.8 to 2.8. The bottom-middle and right panels are scaled from -0.025 to 0.025.

## 5 SIGNAL RECONSTRUCTION

The MAP formalism have been used to reconstruct the large-scale structure of the Universe (e.g. Rybicki & Press 1992; Fisher et al. 1995; Zaroubi et al. 1995). Based on this formalism, we develop a method to reconstruct the 21-cm cosmological signal from the contaminated data. The method relies on the smoothness of the contaminating radiation along the frequency axis and an assumed prior for the correlation properties of the cosmological signal. According to Bayes theorem the conditional probability distribution function for the occurrence of a 3D map,  $\mathbf{T}_c$ , of a 21-cm cosmological signal given an observed data  $\mathbf{T}_o$  is

$$P(\mathbf{T}_c|\mathbf{T}_o) = \frac{P(\mathbf{T}_o|\mathbf{T}_c)P(\mathbf{T}_c)}{P(\mathbf{T}_o)} \propto \exp \left\{ -\frac{1}{2} \sum_u \sum_v [T_r^u [\mathbf{S} + \mathbf{N}]_{u,v}^{-1} T_r^v + (\mathbf{T}_c - \mathbf{W}T_r)^u [\mathbf{S}^{-1} + \mathbf{N}^{-1}]_{u,v} (\mathbf{T}_c - \mathbf{W}T_r)^v] \right\}, \quad (30)$$

where  $\mathbf{u}$  and  $\mathbf{v}$  are position vector indices, and  $\mathbf{W} \equiv \mathbf{S}[\mathbf{S} + \mathbf{N}]^{-1}$  is the Wiener filter. We assume that the signal is approximately a Gaussian random field with an auto-correlation function  $\mathbf{S}$  and that the (uncorrelated) noise is Gaussian with a diagonal correlation function  $\mathbf{N}$  which is  $\mathbf{N}_{u,v} = 0$  for  $\mathbf{u} \neq \mathbf{v}$  and  $\mathbf{N}_{u,u} = \sigma_N^2$  for  $\mathbf{u} = \mathbf{v}$  where  $\sigma_N$  is the noise rms value assumed to be constant (for more details see Appendix A1). We determine  $\mathbf{T}_r$  as the residue of the observed 3D signal,  $\mathbf{T}_o$ , after subtracting the approximated foregrounds. The  $i$ th element along the line-of-sight  $l$  of  $\mathbf{T}_r$  is

$$T_r^{l,i} = T_o^{l,i} - \exp \left\{ \sum_{m=0}^{n_m} b_{l,m} \left[ \ln \left( \frac{\nu_i}{\nu_*} \right) \right]^m \right\}, \quad (31)$$

where we used a polynomial fitting in  $\ln(\nu_i/\nu_*)$  of order  $n_m = 2$  for the foregrounds, and  $(\nu_i/\nu_*)$  is the ratio between the frequency in the  $i$ th bin and  $\nu_* = 150$  MHz. The coefficients of the polynomial,  $b_{l,m}$ , are determined by minimization of the first term of the exponent in the rhs of the conditional probability distribution function, equation (30),

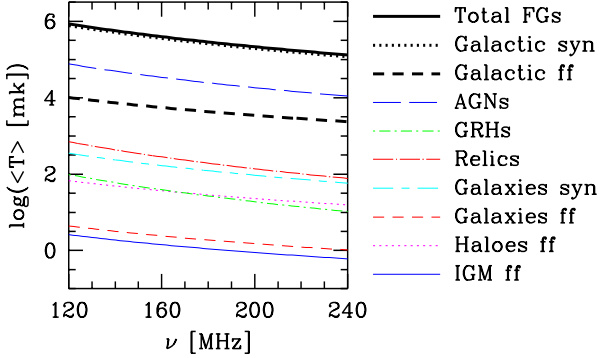


**Figure 4.** The mean brightness temperature of the different foregrounds as a function of frequency. The total galactic and extragalactic foregrounds (thick solid line), the galactic synchrotron emission (thick dotted line), and the galactic free-free emission (thick dashed line), the radio emission from AGNs (thin long-dashed line), radio haloes (thin short-dash dotted line), and radio relics (thin long-dash dotted line), the synchrotron (thin long-dashed short-dashed line) and free-free emissions (thin short-dashed line) from star forming galaxies, and the free-free emission from haloes (thin dotted line), and the diffuse IGM (thin solid line).

either in real space

$$q = \frac{1}{2} \sum_u \sum_v T_r^u [S + N]_{u,v}^{-1} T_r^v \quad (32)$$

or in  $k$ -space

$$\mathcal{Q} = \frac{1}{2} \sum_k \frac{\mathcal{T}_{r,k}^2}{\mathcal{P}_k + \sigma_N^2}, \quad (33)$$

where  $\mathcal{T}_{r,k}$  is the  $\mathbf{k}$  vector element of the 3D Fourier transform of  $\mathbf{T}_r$ , and  $\mathcal{P}_k$  is the 3D power spectrum of the brightness temperature field. To find the best set of  $b_{l,m}$  coefficients, we minimize  $\mathcal{Q}$  by an iterative steepest descent algorithm using the Newton direction as the descent direction

$$d = -(\nabla^2 \mathcal{Q})^{-1} \nabla \mathcal{Q}, \quad (34)$$

where  $\nabla \mathcal{Q}$  and  $\nabla^2 \mathcal{Q}$  are the gradient and the Hessian of  $\mathcal{Q}$ , respectively (for more details see Appendix A2). Then by solving the equation  $\partial P / \partial \mathbf{T}_c = 0$ , one gets the “optimal” signal

$$\mathbf{T}_c = \mathbf{W} \mathbf{T}_r = \mathbf{S} [\mathbf{S} + \mathbf{N}]^{-1} \mathbf{T}_r, \quad (35)$$

or in  $k$ -space,  $\partial P / \partial \mathcal{T}_{c,k} = 0$ ,

$$\mathcal{T}_{c,k} = \left( \frac{\mathcal{P}_k}{\mathcal{P}_k + \sigma_N^2} \right)^\eta \mathcal{T}_{r,k}, \quad (36)$$

where  $\mathcal{T}_{c,k}$  is the  $\mathbf{k}$  element of the 3D Fourier transform of  $\mathbf{T}_c$ ,  $\mathcal{P}_k = \langle \mathcal{P}_k \rangle_k$  is the one-dimensional (1D) mean power spectrum, where  $k = |\mathbf{k}|$ , and the Wiener filter parameter  $\eta$  determines the strength of the Wiener filter. According to the Wiener filter formalism  $\eta = 1$ , but in this case one does not recover all the small scale power since

$$\begin{aligned} \mathcal{P}_k^{\text{rec}} &= \langle (\mathcal{T}_{c,k})^2 \rangle = \left( \frac{\mathcal{P}_k}{\mathcal{P}_k + \sigma_N^2} \right)^2 \langle (\mathcal{T}_{r,k})^2 \rangle \\ &\approx \left( \frac{\mathcal{P}_k}{\mathcal{P}_k + \sigma_N^2} \right)^2 (\mathcal{P}_k + \sigma_N^2) = \left( \frac{\mathcal{P}_k}{\mathcal{P}_k + \sigma_N^2} \right) \mathcal{P}_k. \end{aligned} \quad (37)$$

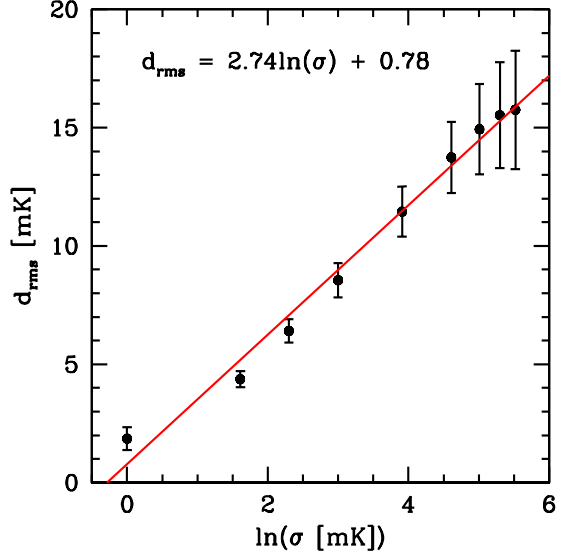


**Figure 7.** The mean  $d_{\text{rms}}$  for all the lines-of-sight in redshift space as a function of the instrumental noise. The full circles are for nine values of instrumental noise,  $\sigma_N = 1, 5, 10, 20, 50, 100, 150, 200$ , and  $250$  mK, with  $\eta = 1$ . The solid line is the best linear fit for these data points in logarithmic scale,  $\langle d_{\text{rms}} \rangle = 2.74 \ln \sigma_N + 0.78$ .

Using  $\eta = 0.5$  eliminates the power suppression at small scales and  $\mathcal{P}_k^{\text{rec}} \approx \mathcal{P}_k$ , but slightly spoils the reconstruction results for each individual line-of-sight.

## 5.1 Results

We assess the ability of the method at reconstructing the cosmological signal using the simulation output around redshift  $z = 10$  in the frequency interval  $\nu = 124.8 - 136.0$  MHz in 256 bins, and for 65536 lines-of-sight. Around this redshift the mean ionization fraction is  $f_{\text{ion}} \approx 0.38$ . The galactic and extragalactic foregrounds are introduced as described in §4. We also add an uncorrelated instrumental random noise component,  $\sigma_N$ , and consider five values from  $\sigma_N = 1$  to  $250$  mK. The method is then applied on noisy and contaminated 3D brightness temperature maps generated from the simulation for redshift space<sup>††</sup>.

To estimate the accuracy of the signal cleaning process we calculated the root-mean-square (rms) of the difference between the true signal from the simulation,  $\mathbf{T}_{\text{true}}^l$ , and the reconstructed signal from the observed data,  $\mathbf{T}_{\text{rec}}^l$ , for all the points along each line-of-sight,  $l$ ,

$$d_{\text{rms}} = \sqrt{\langle (\mathbf{T}_{\text{true}}^l - \mathbf{T}_{\text{rec}}^l)^2 \rangle}. \quad (38)$$

<sup>††</sup> In redshift space the peculiar velocity (deviation from a pure Hubble flow) is taken into account in the relation between the emission and observed frequency.

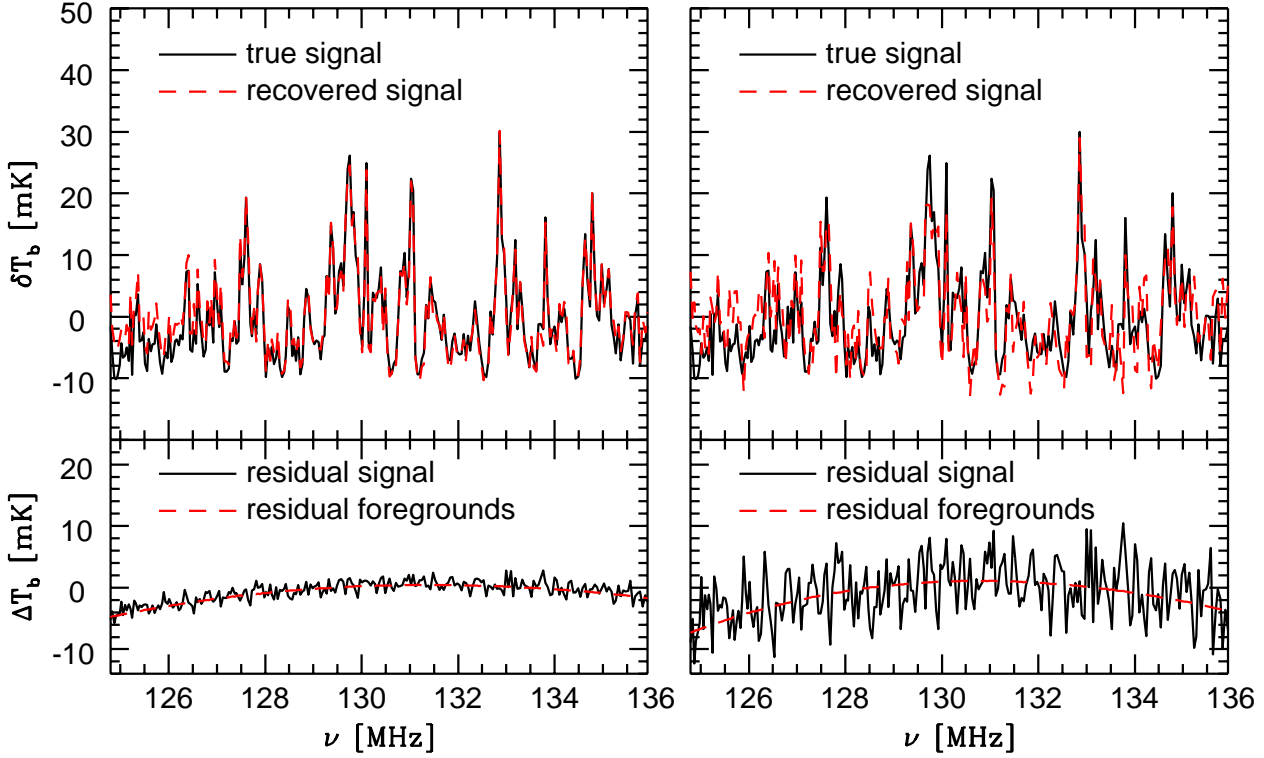


**Figure 8.** A single line-of-sight signal reconstruction in redshift space for  $\sigma_N = 1$  mK and  $d_{rms} = 1.77$  (left panels) and  $\sigma_N = 5$  mK and  $d_{rms} = 4.50$  (right panels). Top panels: the brightness temperature,  $\delta T_b$ , of the true cosmological signal (solid line) and the recovered signal (dashed line). Bottom panels: the residue,  $\Delta T_b$ , between the true and recovered signals (solid line) and between the true and the fitted foregrounds (dashed line). For all cases  $\eta = 0.5$ .

**Table 2.** The mean rms difference,  $d_{rms}$ , between the true cosmological signal from the simulation and the reconstructed signal from the observed data for all lines-of-sight in redshift space. We present the results for five values of instrumental noise where the power index of the reconstructed signal is either  $\eta = 0.5$  or  $\eta = 1$ .

$\sigma_N$ [mK]	$\eta = 0.5$ $\langle d_{rms} \rangle$	$\eta = 1.0$ $\langle d_{rms} \rangle$
1	$1.78 \pm 0.57$	$1.78 \pm 0.57$
5	$4.48 \pm 0.34$	$4.27 \pm 0.39$
20	$10.23 \pm 0.62$	$8.34 \pm 0.77$
100	$20.17 \pm 1.71$	$13.54 \pm 1.61$
250	$27.04 \pm 3.17$	$15.62 \pm 2.71$

In Fig. 7 we present the mean  $d_{rms}$  for all the lines-of-sight at redshift space as a function of the instrumental noise. We calculated  $\langle d_{rms} \rangle$  nine values of noise from  $\sigma_N = 1$  to 250 mK (full circles). We also found the best linear fit in logarithmic scale,  $\langle d_{rms} \rangle = 2.74 \ln \sigma_N + 0.78$ . Since  $\langle d_{rms} \rangle$  has a linear dependence in  $\ln \sigma_N$ , we expect the results of the signal reconstruction process in higher noise levels to be similar to the results in the case of  $\sigma_N = 250$  mK.

In table 2 we present the calculation of the mean  $d_{rms}$  for all the lines-of-sight, for five values of instrumental noise  $\sigma_N = 1, 5, 20, 100$  and 250 mK, and for  $\eta = 0.5$  and 1.

As expected,  $\eta = 1$  gives better  $\langle d_{rms} \rangle$  than  $\eta = 0.5$  and the differences become more significant as the instrumental noise increases. In the case of  $\sigma_N = 1$  mK,  $\langle d_{rms} \rangle$  is higher than the noise level. This happened because we did not take into account the errors in the foreground fitting which has an rms value is of the order of 2 mK. The foreground error rms stays approximately 2 mK also for higher values of  $\sigma_N$  and therefore becomes less significant as the instrumental noise increases.

In Fig. 8 we present an example of a recovered cosmological 21-cm signal compared with the true signal along a line-of-sight and for the noise levels:  $\sigma_N = 1$  mK (top-left panel,  $d_{rms} = 1.77$ ) and  $\sigma_N = 5$  mK (top-right panel,  $d_{rms} = 4.50$ ). The residue between the true and the recovered signals is  $|\Delta T_b| \lesssim 5$  mK for  $\sigma_N = 1$  mK (bottom-left panel) and  $|\Delta T_b| \lesssim 12$  mK for  $\sigma_N = 5$  mK (bottom-right panel). In Fig. 9 we present results for one of the best recovered lines-of-sight, where the rms difference is  $d_{rms} = 0.93$  for  $\sigma_N = 1$  mK and  $d_{rms} = 3.62$  for  $\sigma_N = 5$  mK. The signal residue in this case is  $|\Delta T_b| \lesssim 2$  mK for  $\sigma_N = 1$  mK (bottom-left panel) and  $|\Delta T_b| \lesssim 10$  mK for  $\sigma_N = 5$  mK (bottom-right panel). For all cases in Figs. 8 and 9,  $\eta = 0.5$ . Since the cosmological signal in the simulation box has a mean value of  $\delta T_b = 10.15 \pm 8.61$  mK, there was no point to present the recovered signal for a single line-of-sight for higher values of  $\sigma_N$ .

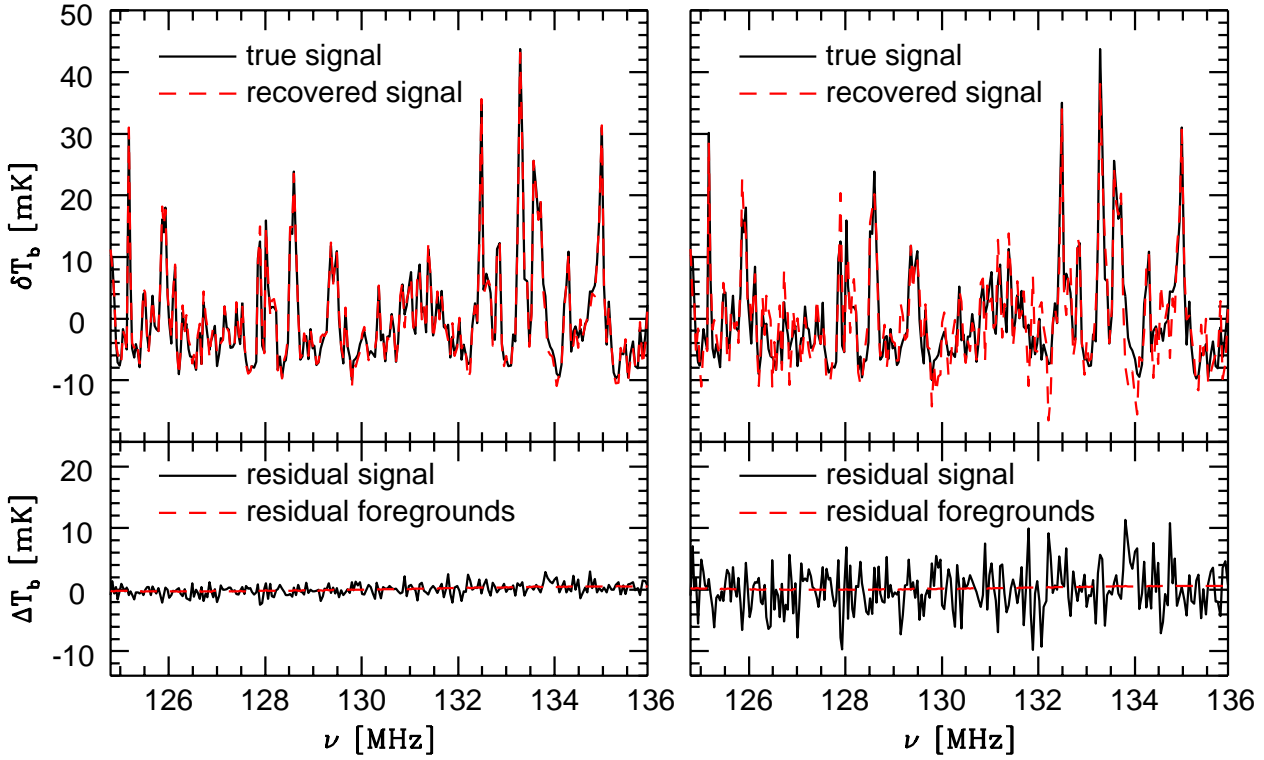


**Figure 9.** Same as Fig. 8, but for one of the best reconstructions, where the rms difference is  $d_{\text{rms}} = 0.93$  for  $\sigma_N = 1$  mK and  $d_{\text{rms}} = 3.62$  for  $\sigma_N = 5$  mK.

We also compute the reconstructed signals for our range of low and high galactic foregrounds. We calculate the mean  $d_{\text{rms}}$  for these cases and found no significant differences to our “optimal” case.

#### 5.1.1 The power spectrum

In Fig. 10 we compare the dimensionless power spectrum,  $\Delta^2(k) \equiv (V/8\pi^3)4\pi k^3 \mathcal{P}_k$ , of the brightness temperature,  $\delta T_b$ , between the true cosmological signal from the simulation (thin solid line), and the reconstructed signal with:  $\sigma_N = 1$  mK (dotted line),  $\sigma_N = 5$  mK (dashed line),  $\sigma_N = 20$  mK (long-dashed line),  $\sigma_N = 100$  mK (dash-dotted line), and  $\sigma_N = 250$  mK (long-dash-dotted line), both for  $\eta = 1$  (thick lines), and  $\eta = 0.5$  (thin lines). As expected from equation (37), for  $\eta = 1$  the power is suppressed at small scales (large wavenumbers  $k$ ), while  $\eta = 0.5$  gives excellent fit for all  $\sigma_N$ . At large scales, where  $\log(k) \lesssim -0.4$ , the size of the simulation box limited the ability to get sufficient statistics in the foreground fitting process. Therefore, the fitted foregrounds include some of the cosmological signal. In Fig. 11 we present a comparison of the true cosmological signal after applying a low-pass filter in  $k$ -space, where  $k \leq 0.1$  h Mpc $^{-1}$ , with the differences between the true and the fitted foregrounds after applying the same low-pass filter, left and middle panels, respectively. One can see the similarity between the two maps which means that for large scales a significant part of the cosmological signal is included in the

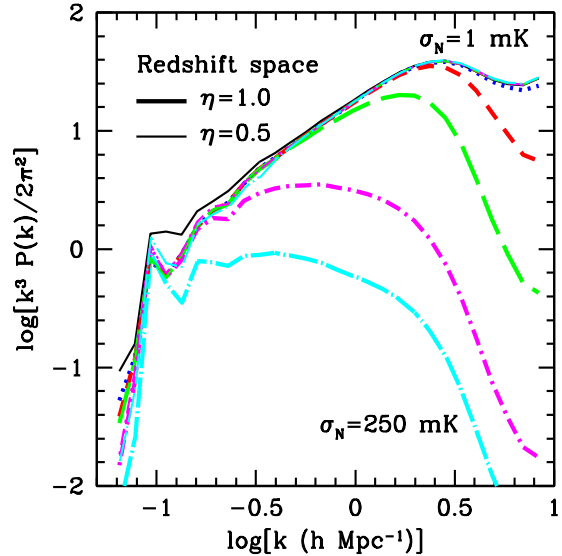


**Figure 10.** The dimensionless power spectrum,  $\Delta^2(k)$ , of the brightness temperature,  $\delta T_b$ , in redshift space, for the cosmological signal from the simulation (thin solid line), and the reconstructed signal with:  $\sigma_N = 1$  mK (dotted line),  $\sigma_N = 5$  mK (dashed line),  $\sigma_N = 20$  mK (long-dashed line),  $\sigma_N = 100$  mK (dash-dotted line), and  $\sigma_N = 250$  mK (long-dash-dotted line), where both  $\eta = 1$  (thick lines), and  $\eta = 0.5$  (thin lines) were used.

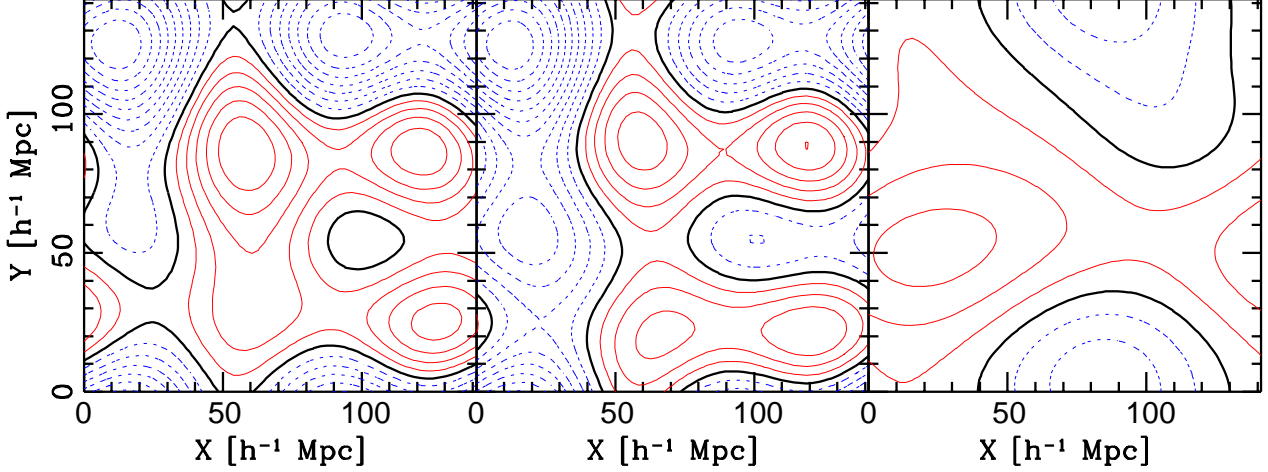


**Figure 11.** The left panel shows a 2D slice of the redshift space 3D map of the true 21-cm cosmological signal from the simulation  $\Delta T_b = \delta T_b - \langle \delta T_b \rangle$  at  $z \approx 10$  after applying a low-pass filter in  $k$ -space, where  $k \leq 0.1 \text{ h Mpc}^{-1}$ . The middle panel shows the differences between the true foregrounds and the fitted foregrounds for the same slice and after applying the same low-pass filter. The difference between the left and middle panels is drawn in the right panel. The thick solid contour indicates  $\Delta T_b = 0 \text{ mK}$ , while the thin solid and dotted contours, respectively, represent the brightness temperatures above and below zero. The contour spacing is  $0.2 \text{ mK}$ , the 2D slice is perpendicular to the lines-of-sight, and  $\sigma_N = 1 \text{ mK}$

fitted foregrounds. To overcome this problem one should use a larger simulation box.

In Fig. 12 we present  $\delta T_b$  the power spectrum in logarithmic scale in the  $k_\perp - k_\parallel$  plane, where  $k_\perp$  and  $k_\parallel$  are the wavenumbers perpendicular and parallel to the lines-of-sight, respectively. The power spectrum of the cosmological signal from the simulation in redshift space is presented in the top-left panel, while the rest of the panels show the power spectrum of the reconstructed signal from the observed data for five values of  $\sigma_N$ : 1 mK (top-middle), 5 mK (top-right), 20 mK (bottom-left), 100 mK (bottom-middle), and 250 mK (bottom-right), where  $\eta = 0.5$  for all cases. One can see that as the noise level grows the power spectrum of the reconstructed signal becomes less and less reliable, especially for large  $k_\perp$  (small scales), where the high instrumental noise eliminates the differences between large and small  $k_\perp$ .

Nusser 2005b suggested to apply the Alcock-Paczynski test on the observed maps of the cosmological signal (cf. Pandey & Bhardwaj 2005; Barkana & Loeb 2005). To do so one must compare the power spectrum in redshift space with power spectrum in real space. Figs. 13 and 14 are the same as Figs. 10 and 12, respectively, but for real space. The dimensionless power spectrum,  $\Delta^2(k)$ , is slightly lower in real space, and the two-dimensional (2D) power spectrum is symmetric in real space and asymmetric in redshift space. We see that a successful application of this test requires noise levels significantly lower than 100 mK.

We also present (Fig. 15) the ratio,  $f_{P(k)} \equiv P_{\text{rec}}(k)/P_{\text{sig}}(k) - 1$ , in the  $k_\perp - k_\parallel$  plane, between the power spectrum of the true cosmological signal,  $P_{\text{sig}}(k)$ , and the power spectrum of the reconstructed signal,  $P_{\text{rec}}(k)$ , where the top and bottom panels are for redshift and real space, respectively. We present the results for the same five values of

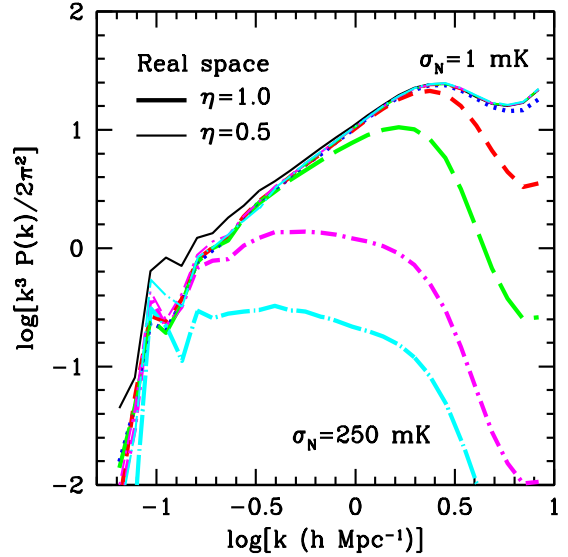


**Figure 13.** The same as Fig. 10 but in real space.

$\sigma_N$ : 1, 5, 20, 100, and 250 mK in five panels from left to right, respectively. For low instrumental noise of  $\sigma_N = 1 \text{ mK}$  the results are reliable with no significant differences on average between the true and reconstructed signals and a variance of  $\sim 1\%$  for  $\log(k) \lesssim 0.5 \text{ [h Mpc}^{-1}]$ , both in real and redshift space. The results for  $\sigma_N = 5 \text{ mK}$  are still reasonably good with differences between the true and reconstructed signals of  $5.0 \pm 8.7\%$  in redshift space and  $8.7 \pm 12.4\%$  in real space, both for  $\log(k) \lesssim 0.5 \text{ [h Mpc}^{-1}]$ . As the instrumental noise increases the differences between the true and reconstructed signals increases and the results becomes less and less reliable (for more details see table 3).



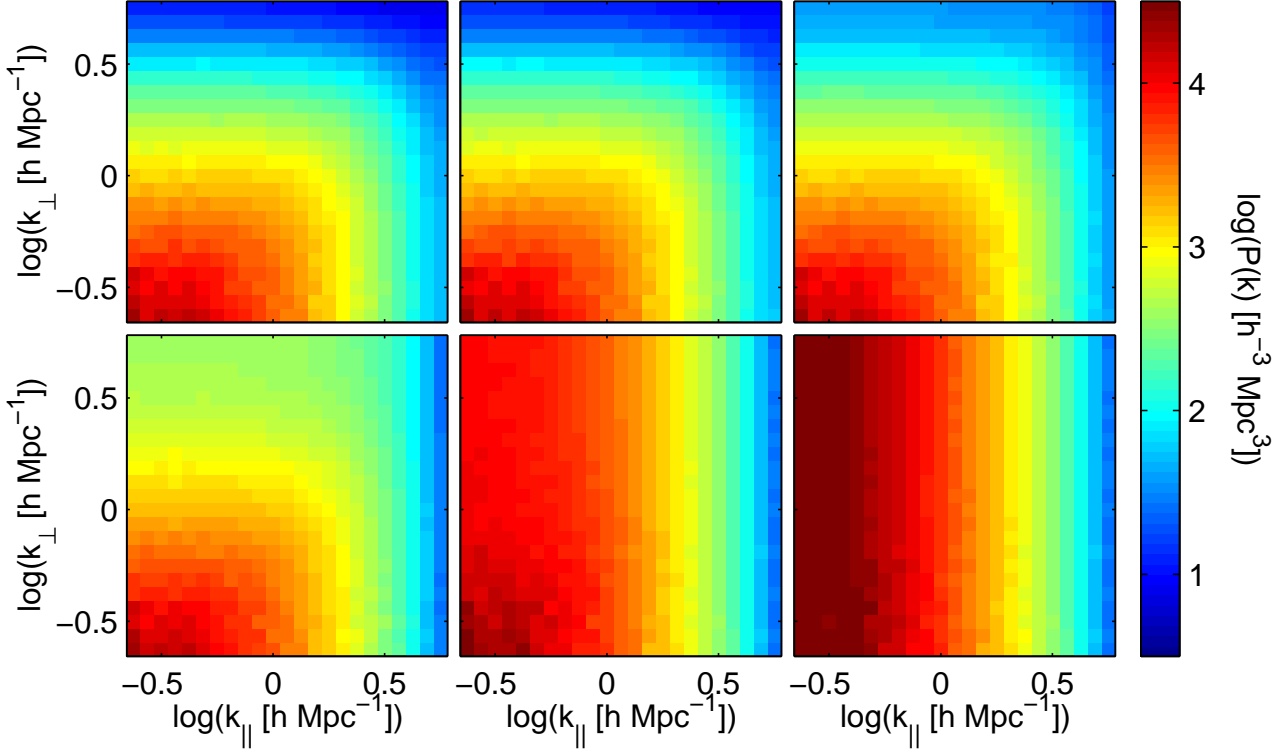


**Figure 12.** The power spectrum in logarithmic scale of the brightness temperature,  $\delta T_b$ , in the  $k_\perp - k_\parallel$  plane, where  $k_\perp$  and  $k_\parallel$  are the wavenumbers perpendicular and the parallel to the lines-of-sight, respectively. The power spectrum of the cosmological signal from the simulation is presented in the top-left panel, while the rest of the panels show the power spectrum of the reconstructed signal from the observed data for five values of  $\sigma_N$ : 1 mK (top-middle), 5 mK (top-right), 20 mK (bottom-left), 100 mK (bottom-middle), and 250 mK (bottom-right). All cases are in redshift space, and  $\eta = 0.5$  was used to reconstruct the signals.

**Table 3.** The mean differences (in percentages) between the true cosmological signal from the simulation and the reconstructed signal from the observed data for five values of  $\sigma_N$  and three different maximal  $\log(k)$ , both in redshift space and real space. The Wiener filter parameter is  $\eta = 0.5$  for all cases.

$\sigma_N$ [mK]	Redshift space			Real space		
	$\log(k)$ [h Mpc $^{-1}$ ]					
	$\lesssim 0.03$	$\lesssim 0.21$	$\lesssim 0.51$	$\lesssim 0.03$	$\lesssim 0.21$	$\lesssim 0.51$
1	$-0.4 \pm 0.9$	$-0.3 \pm 0.8$	$0.0 \pm 0.8$	$-0.1 \pm 1.2$	$-0.1 \pm 1.0$	$0.3 \pm 1.0$
5	$0.2 \pm 1.4$	$0.8 \pm 1.7$	$5.0 \pm 8.7$	$0.8 \pm 1.9$	$1.8 \pm 2.2$	$8.7 \pm 12.4$
20	$9.4 \pm 8.7$	$17.6 \pm 18.7$	$71.7 \pm 114.5$	$17.1 \pm 11.6$	$29.3 \pm 21.3$	$100.7 \pm 124.7$
100	$180.5 \pm 159.0$	$291.1 \pm 345.0$	$912.3 \pm 1797.4$	$254.2 \pm 143.1$	$350.4 \pm 300.0$	$885.6 \pm 1568.6$
250	$574.9 \pm 640.3$	$881.2 \pm 1336.1$	$2627.0 \pm 6452.1$	$620.4 \pm 500.5$	$821.7 \pm 1018.4$	$2060.9 \pm 4841.7$

### 5.1.2 The Minkowski functionals

The morphology of the total gas and the neutral hydrogen distributions during the cosmological epoch of reionization can be quantified with Minkowski functionals (MFs) of isodensity surfaces. Gleser et al. (2006) suggested the MFs as a means of investigating the reionization epoch. In Figs. 16 and 17 we present the MFs from the 21-cm cosmological signal in redshift and real space, respectively, where  $V_0(\nu)$  is the volume of regions with brightness temperature above the threshold  $T_{\text{thr}}$ ,  $V_1(\nu)$  is a measure of the surface area of the boundary,  $V_2(\nu)$  is the mean curvature over the surface,

and  $V_3(\nu)$  is the Euler characteristic,  $\chi$ . We compare the MFs of the true cosmological signal brightness temperature (thin solid line), and the reconstructed signal with:  $\sigma_N = 1$  mK (dotted line),  $\sigma_N = 5$  mK (dashed line),  $\sigma_N = 20$  mK (long-dashed line),  $\sigma_N = 100$  mK (dash-dotted line), and  $\sigma_N = 250$  mK (long-dash-dotted line), both for  $\eta = 1$  (thick lines), and  $\eta = 0.5$  (thin lines). Since the MFs are sensitive to the residual noise and foreground contamination, we smooth the 21-cm maps with a Gaussian filter of width  $0.55 \text{ h}^{-1} \text{ Mpc}$  before applying the MFs computing code to them.

A comparison of the  $V_0$  curves in the figures shows that the reconstructed maps have fewer regions with high bright-

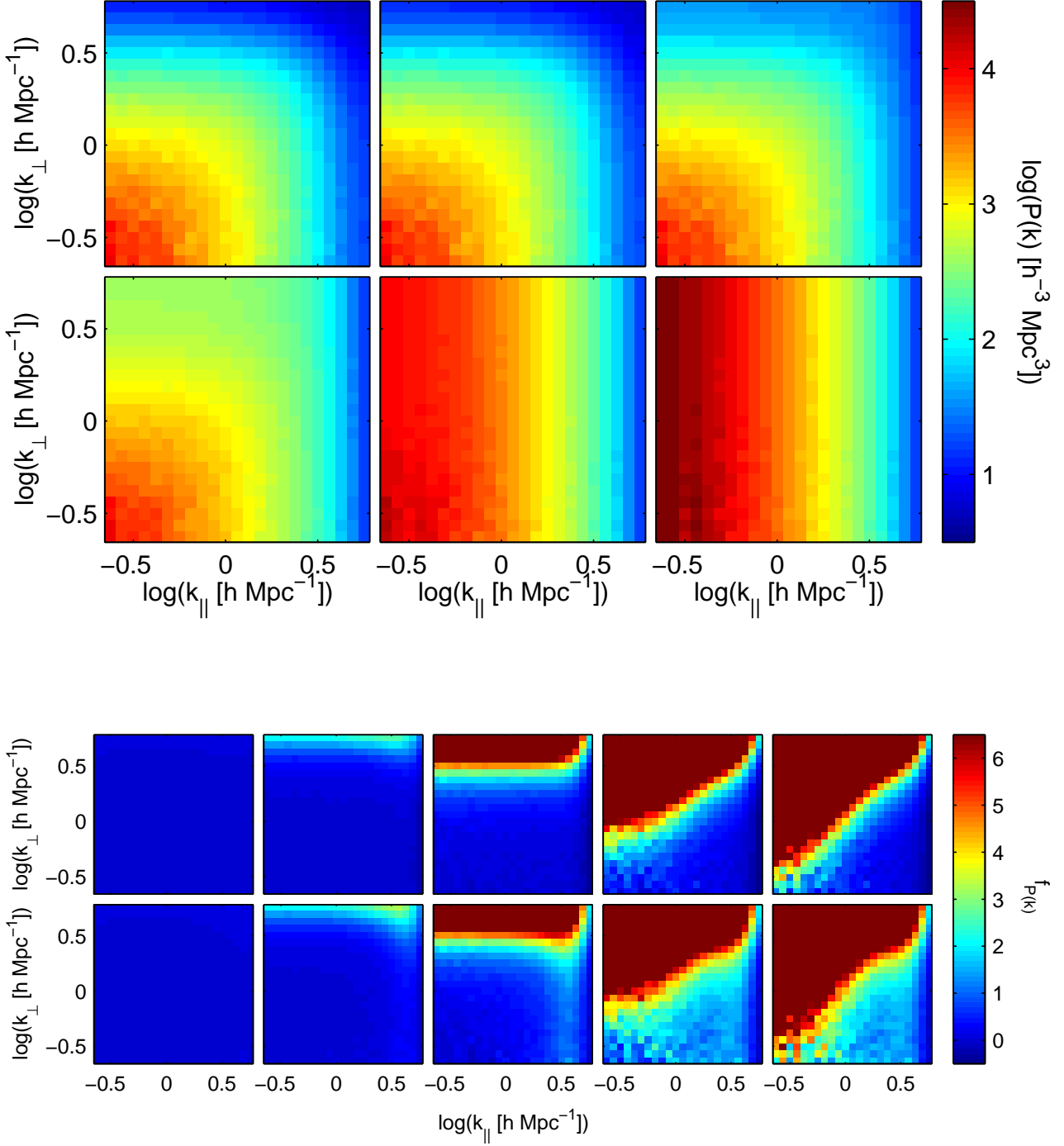


**Figure 15.** The ratio,  $f_{P(k)} \equiv P_{\text{rec}}(k)/P_{\text{sig}}(k) - 1$ , between the recovered and true signal power spectrum in redshift space (top panels) and real space (bottom panels). The results for five values of  $\sigma_N$ : 1, 5, 20, 100, and 250 mK are presented in five panels from left to right, respectively. For all cases  $\eta = 0.5$ .

ness temperature than the true cosmological signal. This effect increases with the noise rms  $\sigma_N$ . Both in real and redshift space,  $\eta = 0.5$  perform better than  $\eta = 1$  at recovering the true MFs. In any case, the recovery of the MFs is reasonable for  $\sigma_N = 1$  and 5 mK, suggesting that in the future, when the noise level will be reduced to  $\sigma_N \approx 5$  mK, the MFs could be used to distinguish between different stages

of ionization and between different reionization scenarios as advocated by Gleser et al. (2006).



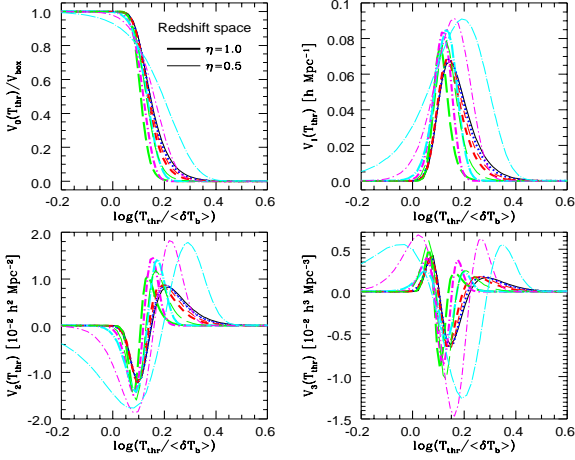


**Figure 16.** The Minkowski functionals in redshift space of the true cosmological signal brightness temperature (thin solid line), and the reconstructed signal with:  $\sigma_N = 1$  mK (dotted line),  $\sigma_N = 5$  mK (dashed line),  $\sigma_N = 20$  mK (long-dashed line),  $\sigma_N = 100$  mK (dash-dotted line), and  $\sigma_N = 250$  mK (long-dash-dotted line), where both  $\eta = 1$  (thick lines), and  $\eta = 0.5$  (thin lines) were used.

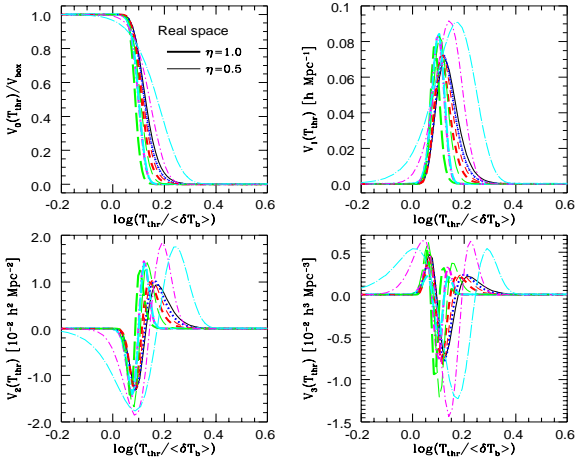


**Figure 17.** The same as Fig. 16 but in real space.

## 6 DISCUSSION

Maps of 21-cm radiation from diffuse H I before and during the epoch of reionization are potentially our only direct probe of the Universe in the dark ages. From this point of view the efforts invested in modeling this radiation and in attempts to observe it are worthwhile. Redshifted 21-cm maps are likely to constrain the early stages of star and galaxy formation and also the state of the diffuse H I before any light emitting object had formed. Decoupling of the H I spin temperature,  $T_s$ , from the CMB temperature,  $T_{\text{CMB}}$ , is necessary for observing redshifted 21-cm (either in absorption or in

emission). In the absence of any heating mechanisms, the kinetic gas temperature,  $T_k$ , drops below  $T_{\text{CMB}}$  at redshifts  $z \lesssim 100$ . For  $z \gtrsim 20$  the Universe is dense enough so that atom-atom collisions are still efficient at bringing  $T_s$  down towards  $T_k$ . However, even in the absence of luminous structure, the gas temperature could be raised above the CMB if the dark matter could decay or annihilate (e.g. Ripamonti, Mapelli & Ferrara 2007). For example, neutralinos, if they are the dark matter particles, produce sufficient electron-positron  $e^-e^+$  pairs by self-annihilations (Myers & Nusser 2007). High energy photons generated by inverse Compton scattering of CMB photons, could then photo-heat the gas to kinetic temperatures above  $T_{\text{CMB}}$ . In this case, the gas is never seen in absorption. Therefore, 21-cm maps could in principle also constrain the nature of the dark matter particle.

The 21-cm cosmological signal will suffer from several sources of contamination. In the first part of this work we model the contamination which is produced by foreground radiation emitted from galactic and extragalactic sources, and produced 3D contamination maps. The foregrounds model includes synchrotron and free-free emission from our Galaxy and seven extragalactic foregrounds: radio point sources which relate to AGN activity, radio haloes and radio relics from massive dark matter haloes with mass of  $M_{\text{halo}} \gtrsim 5 \times 10^{14} M_{\odot}$ , synchrotron and free-free emission from star forming galaxies, and free-free emission from ionized hydrogen dark matter haloes and diffuse IGM. The most significant foreground is the galactic synchrotron which cause  $\sim 90\%$  of the contamination on average. The galactic free-free contributes another 1-2% to the total contamination. The AGN radio point sources produce  $\sim 10\%$  of the total contamination on average, but can reach  $\sim 25\%$  at high galactic latitudes, where the minimum brightness temperature of the diffuse galactic emission drops to  $\sim 200$  K. Radio haloes and radio relics are also significant foregrounds, but since they appear only in rich galaxy clusters, they are rare and should appear only as spots in individual lines-of-sight. The remaining extragalactic foregrounds are less significant and contribute less than 1% to the total contamination.

In the second part we add the 3D contamination maps and an instrumental random noise to the maps of the cosmological 21-cm signal, and apply a reconstruction method based on a Bayesian statistical approach. We take advantage of the foregrounds' smooth dependence on frequency in contrast to the “noisy” signal. Then we derive an appropriate Wiener filter to extract the cosmological signal from the residual brightness temperature obtained after subtracting the approximated foregrounds from the observed data. We also introduce a power index  $\eta$  which determines the strength of the Wiener filter. The Wiener filter obtained directly from Bayesian statistics has  $\eta = 1$ , but using  $\eta = 0.5$  eliminates the power suppression at small scales. For low instrumental noise we were able to get reasonable reconstruction of the cosmological signal for each line-of-sight, where  $d_{\text{rms}} \approx 1.7 \pm 0.6$  for  $\sigma_N = 1$  mK, and  $d_{\text{rms}} \approx 4.2 \pm 0.4$  for  $\sigma_N = 5$  mK. We checked the reconstruction of the statistical measurements of the power spectrum and the MFs. The 1D power spectrum was nicely reconstructed for all values of the instrumental noise up to 250 mK, while the 2D power

spectrum and the MFs were reconstructed reasonably well only for noise levels significantly lower than 100 mK.

## ACKNOWLEDGMENTS

LG and AN acknowledge the support of the Asher Space Research Institute and the German Israeli Foundation for the Development of Research. AJB acknowledges support from the Gordon & Betty Moore Foundation.

## REFERENCES

- Banday A. J., Wolfendale A. W., 1990, MNRAS, 245, 182  
 Banday A. J., Wolfendale A. W., 1991, MNRAS, 248, 705  
 Barkana R., Loeb A., 2005, ApJ, 624, L65  
 Bennett C. L. et al. , 2003, ApJS, 148, 97  
 Benson A. J., Nusser A., Sugiyama N., Lacey C. G., 2001, MNRAS, 320, 153  
 Benson A. J., Sugiyama N., Nusser A., Lacey C. G., 2006, MNRAS, 369, 1055  
 Blanton M. R. et al. , 2001, AJ, 121, 2358  
 Blanton M. R. et al. , 2003, ApJ, 592, 819  
 Bridle A. H., 1967, MNRAS, 136, 219  
 Cane H. V., 1979, MNRAS, 189, 465  
 Cassano R., Brunetti G., Setti G., 2006, MNRAS, 369, 1577  
 Chuzhoy L., Zheng Z., 2007, ApJ, 670, 912  
 Ciardi B., Madau P., 2003, ApJ, 596, 1  
 Cooray A., Furlanetto S. R., 2004, ApJ, 606, L5  
 Di Matteo T., Ciardi B., Miniati F., 2004, MNRAS, 355, 1053  
 Di Matteo T., Perna R., Abel T., Rees M., 2002, ApJ, 564, 576  
 Dunlop J. S., Peacock J. A., 1990, MNRAS, 247, 19  
 Eke V. R., Navarro J. F., Steinmetz M., 2001, ApJ, 554, 114  
 Enßlin T. A., Gopal-Krishna, 2001, A&A, 366, 26  
 Ferguson H. C. et al. , 2004, ApJ, 600, L107  
 Fisher K. B., Lahav O., Hoffman Y., Lynden-Bell D., Zaroubi S., 1995, MNRAS, 272, 885  
 Giovannini G., Feretti L., 2004, JKAS, 37, 323  
 Gleser L., Nusser A., Ciardi B., Desjacques V., 2006, MNRAS, 370, 1329  
 Gnedin N. Y., Shaver P. A., 2004, ApJ, 608, 611  
 Haslam C. G. T., Klein U., Salter C. J., Stoffel H., Wilson W. E., Cleary M. N., Cooke D. J., Thomasson P., 1981, A&A, 100, 209  
 Haslam C. G. T., Salter C. J., Stoffel H., Wilson, W. E., 1982, A&AS, 47, 1  
 Haverkorn M., Katgert P., de Bruyn A. G., 2003, A&A, 403, 1031  
 Heiles C., 2001, in Woodward C. E., Bica M. D., Shull J. M., eds, ASP Conf. Ser. Vol. 231, Tetrans 4: Galactic Structure, State and the Interstellar Medium, Astron. Soc. Pac., San Francisco, p. 294  
 Helmi A., Navarro J. F., Meza A., Steinmetz M., Eke V. R., 2003, ApJ, 592, L25  
 Hoeft M., Brüggen M., Yepes G., 2004, MNRAS, 347, 389  
 Hummel E., 1991, A&A, 251, 442  
 Ibat R. A., Irwin M. J., Lewis G. F., Ferguson A. M. N., Tanvir N., 2003, MNRAS, 340, L21  
 Jelic V. et al. , 2008, MNRAS, 389, 1319  
 Kempner J. C., Blanton E. L., Clarke T. E., Enßlin T. A., Johnston-Hollitt M., Rudnick L., 2004, in *The Riddle of Cooling Flows in Galaxies and Clusters of Galaxies* Conference Note  
 Lang K. R., 1999, *Astrophysical Formulae*, Vol. 1 (Berlin:Springer)  
 Lawson K. D., Mayer C. J., Osborne J. L., Parkinson M. L., 1987, MNRAS, 225, 307  
 Madau P., Meiksin A., Rees M. J., 1997, ApJ, 475, 429  
 Madau P., Rees M. J., Salvati M., 2004, MNRAS, 351, 169  
 McQuinn M., Zahn O., Zaldarriaga M., Hernquist L., Furlanetto S. R., 2006, ApJ, 653, 815  
 Meiksin A., 2007, submitted to *Reviews of Modern Physics* (arXiv:0711.3358)  
 Morales M. F., Hewitt J., 2004, ApJ, 615, 7  
 Morales M. F., Bowman J. D., Hewitt J., 2006, ApJ, 648, 767  
 Myers Z., Nusser A., 2007, MNRAS, 384, 727  
 Navarro J. F., Frenk C. S., White S. D. M., 1996, ApJ, 462, 563  
 Navarro J. F., Frenk C. S., White S. D. M., 1997, ApJ, 490, 493  
 Navarro J. F., Hayashi E., Power C., Jenkins A. R., Frenk C. S., White S. D. M., Springel V., Stadel J., Quinn T. R., 2004, MNRAS, 349, 1039  
 Norman C. et al. , 2004, ApJ, 607, 721  
 Nusser A., 2005a, MNRAS, 359, 183  
 Nusser A., 2005b, MNRAS, 364, 743  
 Oh S. P., Mack K. J., 2003, MNRAS, 346, 8710  
 Pacholczyk A. G., 1970, *Radio Astrophysics*, Freeman & Co., San Francisco  
 Pandey B., Bharadwaj S., 2005, MNRAS, 358, 939  
 Peacock J. A., 1985, MNRAS, 217, 601  
 Platania P., Burigana C., Maino D., Caserini E., Bersanelli M., Cappellini B., Mennella A., 2003, A&A, 410, 847  
 Ranalli P., Comastri A., Setti G., 2005, A&A, 440, 23  
 Reich P., Reich, W., 1988, A&A, 74, 7  
 Reich P., Testori J. C., Reich, W., 2001, A&A, 376, 861  
 Ricotti, M., Ostriker, J.P., 2004, MNRAS, 352, 547  
 Ripamonti E., Mapelli M., Ferrara A., 2007, MNRAS, 374, 1067  
 Rybicki G. B., Press W. H., 1992, ApJ, 398, 169  
 Rybicki G. B., Lightman A. P., 1979, *Radiative Processes in Astrophysics*, Wiley, New York  
 Santos M. G., Cooray A., Knox L., 2005, ApJ, 625, 575  
 Shaver P. A., Windhorst R. A., Madau P., de Bruyn A. G., 1999, A&A, 345, 380  
 Shen S., Mo H. J., White S. D. M., Blanton M. R., Kauffmann G., Voges W., Brinkmann J., Csabai I., 2003, MNRAS, 343, 978  
 Sheth R. K., Tormen G., 1999, MNRAS, 308, 119  
 Spergel D. N. et al. , 2007, ApJS, 170, 377  
 Takeuchi T. T., Yoshikawa K., Ishii T. T., 2003, ApJ, 587, L89  
 Takeuchi T. T., Yoshikawa K., Ishii T. T., 2004, ApJ, 606, L171  
 Tegmark M., Eisenstein D. J., Hu W., de Oliveira-Costa A., 2000, ApJ, 530, 133  
 Thomas R. M., Zaroubi S., 2007, MNRAS, 384, 1080  
 Tillmann R., 2002, Dissertation, Ruhr-Universität, Bochum  
 Wang X., Tegmark M., Santos M. G., Knox L., 2006, ApJ, 650, 529  
 Willis A. G., Oosterbaan C. E., Lepole R. S., de Ruiter H. R., Strom R. G., Valentijn E. A., Katgert P., Katgert-Merkelijn J. K., 1977, in Jauncey D. L., ed, *IAU Symposium*, No. 74, Radio Astronomy and Cosmology, D. Reidel Publishing Co., Holland, p. 39  
 Willott C. J., Rawlings S., Blundell K. M., Lacy M., Eales S. A., 2001, MNRAS, 322, 536  
 Yanny B. et al. , 2003, ApJ, 588, 824  
 Zaldarriaga M., Furlanetto S. R., Hernquist L., 2004, ApJ, 608, 622  
 Zaroubi S., Hoffman Y., Fisher K. B., Lahav O., 1995, ApJ, 449, 446  
 Zaroubi S., Thomas R. M., Sugiyama N., Silk J., 2007, MNRAS, 375, 1269

## APPENDIX A: THE METHOD OF SIGNAL RECONSTRUCTION

The maximum a-posteriori probability (MAP) formalism have been used to reconstruct the large-scale structure of the Universe (e.g. Rybicki & Press 1992; Zaroubi et al. 1995; Fisher et al. 1995). Based on this formalism, we develop a method to reconstruct the weak 21-cm cosmological signal from the contaminated noisy data. The method relies on the smoothness of the contaminating radiation along the frequency axis and an assumed prior for the correlation properties of the cosmological signal.

### A1 The conditional probability

Let  $P(\mathbf{s}|\mathbf{d})$  be the conditional probability distribution function to get the signal vector  $\mathbf{s}$  given the data vector  $\mathbf{d}$ . The MAP method estimates  $\mathbf{s}$  by maximization of  $P(\mathbf{s}|\mathbf{d})$ . According to Bayes theorem

$$P(\mathbf{s}|\mathbf{d}) = \frac{P(\mathbf{d}|\mathbf{s})P(\mathbf{s})}{P(\mathbf{d})}. \quad (\text{A1})$$

Since the maximization is on  $\mathbf{s}$ , the denominator  $P(\mathbf{d})$  can be ignored. In addition to the true signal, the data  $\mathbf{d}$  contains contamination from different foreground sources and a random (instrumental) noise. Here  $\mathbf{c}$  represents the fit to the total contamination. The  $i$ th element of the contamination along a line-of-sight  $l$  is

$$c_{l,i} = \exp \left( \sum_{m=0}^{n_m} b_{l,m} x_{l,i}^m \right) \quad (\text{A2})$$

where we use a polynomial approximation in  $x_{l,i} = \ln(\nu_{l,i}/\nu_*)$  of order  $n_m$ ,  $\nu_{l,i}$  is the frequency at position  $i$  along the line-of-sight  $l$ ,  $\nu_*$  is a constant frequency, and  $b_{l,m}$  are the polynomial coefficients.<sup>††</sup> Usually, the frequency  $\nu_{l,i} \equiv \nu_i$  is the same for all  $l$ 's, and therefore, the vector  $\mathbf{x}$  contains  $n_l$  times the vector  $\mathbf{x}_i = \ln(\nu_i/\nu_*)$ , where  $n_l$  is the number of lines-of-sight. We determine the residue vector  $\mathbf{y} = \mathbf{d} - \mathbf{c}$  as the residual data  $\mathbf{d}$  after subtraction of the approximated contaminations  $\mathbf{c}$ . So ideally,  $\mathbf{y}$  contains only the true signal and the random noise.

Assuming that the signal is approximately a Gaussian random field with an auto-correlation matrix  $\mathbf{S}$ , the probability function of  $\mathbf{s}$  is

$$P(\mathbf{s}) = \exp \left( -\frac{1}{2} \mathbf{s}^T \mathbf{S}^{-1} \mathbf{s} \right). \quad (\text{A3})$$

Further, assuming a Gaussian noise matrix  $\mathbf{N}$ , the probability for  $\mathbf{d}$  giving  $\mathbf{s}$  is

$$P(\mathbf{d}|\mathbf{s}) = \exp \left[ -\frac{1}{2} (\mathbf{y} - \mathbf{s})^T \mathbf{N}^{-1} (\mathbf{y} - \mathbf{s}) \right]. \quad (\text{A4})$$

In the following we assume  $\mathbf{N} = \mathbf{I}\sigma_N$ , where  $\sigma_N$  is the noise rms and  $\mathbf{I}$  is the identity matrix.

<sup>††</sup> We use two indices  $l$  and  $i$  to determine the position of each element in the vectors  $\mathbf{c}$  and  $\mathbf{x}$ . One can replace  $l$  and  $i$  with a single index  $j$  where  $j = n_l(l-1) + i$  and  $n_l$  is the number of frequencies along a single line-of-sight.

Using the above probability functions (equations (A3) & (A4)), the probability  $P(\mathbf{s}|\mathbf{d})$  is proportional to

$$\begin{aligned} P(\mathbf{s}|\mathbf{d}) &\propto P(\mathbf{d}|\mathbf{s})P(\mathbf{s}) \\ &= \exp \left\{ -\frac{1}{2} [(\mathbf{y} - \mathbf{s})^T \mathbf{N}^{-1} (\mathbf{y} - \mathbf{s}) + \mathbf{s}^T \mathbf{S}^{-1} \mathbf{s}] \right\} \\ &= \exp \left\{ -\frac{1}{2} [\mathbf{y}^T \mathbf{N}^{-1} \mathbf{y} + \mathbf{s}^T (\mathbf{S}^{-1} + \mathbf{N}^{-1}) \mathbf{s} \right. \\ &\quad \left. - \mathbf{y}^T \mathbf{N}^{-1} \mathbf{s} - \mathbf{s}^T \mathbf{N}^{-1} \mathbf{y}] \right\}, \\ &= \exp \left\{ -\frac{1}{2} [\mathbf{y}^T (\mathbf{S} + \mathbf{N})^{-1} \mathbf{y} + \mathbf{s}^T (\mathbf{S}^{-1} + \mathbf{N}^{-1}) \mathbf{s} \right. \\ &\quad + \mathbf{y}^T \mathbf{N}^{-1} \mathbf{S} (\mathbf{S} + \mathbf{N})^{-1} \mathbf{y} \\ &\quad - \mathbf{y}^T \mathbf{S} (\mathbf{S} + \mathbf{N})^{-1} (\mathbf{S}^{-1} + \mathbf{N}^{-1}) \mathbf{s} \\ &\quad \left. - \mathbf{s}^T (\mathbf{S}^{-1} + \mathbf{N}^{-1}) \mathbf{S} (\mathbf{S} + \mathbf{N})^{-1} \mathbf{y}] \right\}, \end{aligned} \quad (\text{A5})$$

where we use the matrix identity

$$\begin{aligned} \mathbf{N}^{-1} &= \mathbf{N}^{-1} (\mathbf{S} + \mathbf{N}) (\mathbf{S} + \mathbf{N})^{-1} = (\mathbf{N}^{-1} \mathbf{S} + \mathbf{I}) (\mathbf{S} + \mathbf{N})^{-1} \\ &= \mathbf{N}^{-1} \mathbf{S} (\mathbf{S} + \mathbf{N})^{-1} + (\mathbf{S} + \mathbf{N})^{-1} \end{aligned} \quad (\text{A6})$$

for the first term in the rhs of the equation, and

$$(\mathbf{S}^{-1} + \mathbf{N}^{-1})^{-1} = \mathbf{S} (\mathbf{S} + \mathbf{N})^{-1} \mathbf{N} = \mathbf{N} (\mathbf{S} + \mathbf{N})^{-1} \mathbf{S} \quad (\text{A7})$$

for the third and the fourth terms in the rhs of the equation. Next we again use the identity in equation (A7) for the third term in the rhs of equation (A5), and get

$$\begin{aligned} P(\mathbf{s}|\mathbf{d}) &\propto \exp \left\{ -\frac{1}{2} [\mathbf{y}^T (\mathbf{S} + \mathbf{N})^{-1} \mathbf{y} + \mathbf{s}^T (\mathbf{S}^{-1} + \mathbf{N}^{-1}) \mathbf{s} \right. \\ &\quad + \mathbf{y}^T \mathbf{S} (\mathbf{S} + \mathbf{N})^{-1} (\mathbf{S}^{-1} + \mathbf{N}^{-1}) \mathbf{S} (\mathbf{S} + \mathbf{N})^{-1} \mathbf{y} \\ &\quad - \mathbf{y}^T \mathbf{S} (\mathbf{S} + \mathbf{N})^{-1} (\mathbf{S}^{-1} + \mathbf{N}^{-1}) \mathbf{s} \\ &\quad \left. - \mathbf{s}^T (\mathbf{S}^{-1} + \mathbf{N}^{-1}) \mathbf{S} (\mathbf{S} + \mathbf{N})^{-1} \mathbf{y}] \right\} \\ &= \exp \left\{ -\frac{1}{2} [\mathbf{y}^T (\mathbf{S} + \mathbf{N})^{-1} \mathbf{y} + \mathbf{s}^T (\mathbf{S}^{-1} + \mathbf{N}^{-1}) \mathbf{s} \right. \\ &\quad + (\mathbf{S} (\mathbf{S} + \mathbf{N})^{-1} \mathbf{y})^T (\mathbf{S}^{-1} + \mathbf{N}^{-1}) (\mathbf{S} (\mathbf{S} + \mathbf{N})^{-1} \mathbf{y}) \\ &\quad - (\mathbf{S} (\mathbf{S} + \mathbf{N})^{-1} \mathbf{y})^T (\mathbf{S}^{-1} + \mathbf{N}^{-1}) \mathbf{s} \\ &\quad \left. - \mathbf{s}^T (\mathbf{S}^{-1} + \mathbf{N}^{-1}) (\mathbf{S} (\mathbf{S} + \mathbf{N})^{-1} \mathbf{y})] \right\} \\ &= \exp \left\{ -\frac{1}{2} [\mathbf{y}^T (\mathbf{S} + \mathbf{N})^{-1} \mathbf{y} + (\mathbf{s} - \mathbf{S} (\mathbf{S} + \mathbf{N})^{-1} \mathbf{y})^T \right. \\ &\quad \left. \times (\mathbf{S}^{-1} + \mathbf{N}^{-1}) (\mathbf{s} - \mathbf{S} (\mathbf{S} + \mathbf{N})^{-1} \mathbf{y})] \right\}, \end{aligned} \quad (\text{A8})$$

### A2 Fitting the contamination

The fitting process of the total contamination,  $\mathbf{c}$ , depends on two assumptions: (i) the signal is much weaker than the total contamination, and (ii) the contamination has a smooth frequency spectrum while the signal is rapidly changing in frequency. Once these assumptions are valid, we can switch between the signal and the contamination, and treat the contamination as the desirable signal and the signal as an additional random noise. Now, the polynomial coefficients,  $b_{l,m}$ , can be calculated by minimization of the first term of the exponent at the rhs of the conditional probability dis-

tribution function (equation (A8))

$$q = \frac{1}{2} \sum_{l=1}^{n_l} \sum_{i=1}^{n_i} \sum_{l'=1}^{n_l} \sum_{i'=1}^{n_i} (d_{l,i} - c_{l,i}) (\mathbf{S} + \mathbf{N})_{l,i,l',i'}^{-1} (d_{l',i'} - c_{l',i'}), \quad (\text{A9a})$$

$$\frac{\partial q}{\partial b_{l,m}} = - \sum_{i=1}^{n_i} \sum_{l'=1}^{n_l} \sum_{i'=1}^{n_i} x_{l,i}^m c_{l,i} (\mathbf{S} + \mathbf{N})_{l,i,l',i'}^{-1} (d_{l',i'} - c_{l',i'}), \quad (\text{A9b})$$

$$\begin{aligned} \frac{\partial^2 q}{\partial b_{l,m} \partial b_{l',n}} = & \sum_{i=1}^{n_i} \sum_{i'=1}^{n_i} \left[ x_{l,i}^m c_{l,i} (\mathbf{S} + \mathbf{N})_{l,i,l',i'}^{-1} x_{l',i'}^n c_{l',i'} \right. \\ & \left. - \delta_{l-l'} x_{l,i}^{m+n} c_{l,i} (\mathbf{S} + \mathbf{N})_{l,i,l',i'}^{-1} (d_{l',i'} - c_{l',i'}) \right] \end{aligned} \quad (\text{A9c})$$

where  $i$  and  $i'$  are the frequency position indices, from 1 to  $n_i$ , along the lines-of-sight  $l$  and  $l'$ , respectively. The number of lines-of-sight is  $n_l$ , and  $\delta_{l-l'}$  is the Kronecker delta which equal one for  $l = l'$  and zero otherwise. Equations (A9b) and (A9c) are the elements of the gradient and Hessian, respectively, where there are  $n_m + 1$  coefficients,  $b_{l,m}$ , for each line-of-sight.

The minimization can be calculated also in Fourier-space

$$\mathcal{Q} = \frac{1}{2} \sum_k \frac{\mathcal{Y}_k^2}{\mathcal{P}_k + \sigma_N^2} = \frac{1}{2} \sum_k \frac{(\mathcal{D}_k - \mathcal{C}_k)^2}{\mathcal{P}_k + \sigma_N^2}, \quad (\text{A10a})$$

$$\frac{\partial \mathcal{Q}}{\partial b_{l,m}} = - \sum_k \frac{\mathcal{F}_k(\mathbf{z}_m) (\mathcal{D}_k - \mathcal{C}_k)}{\mathcal{P}_k + \sigma_N^2}, \quad (\text{A10b})$$

$$\begin{aligned} \frac{\partial^2 \mathcal{Q}}{\partial b_{l,m} \partial b_{l',n}} = & \sum_k \left[ \frac{\mathcal{F}_k(\mathbf{z}_m) \mathcal{F}_k(\mathbf{z}_n)}{\mathcal{P}_k + \sigma_N^2} \right. \\ & \left. - \delta_{l-l'} \frac{\mathcal{F}_k(\mathbf{z}_{m+n}) (\mathcal{D}_k - \mathcal{C}_k)}{\mathcal{P}_k + \sigma_N^2} \right], \end{aligned} \quad (\text{A10c})$$

where  $\mathcal{Y}_k$ ,  $\mathcal{D}_k$ , and  $\mathcal{C}_k$  are the  $k$  elements of the Fourier transform of  $\mathbf{y}$ ,  $\mathbf{d}$ , and  $\mathbf{c}$ , respectively,  $\mathcal{P}_k$  is the field power spectrum, and  $\mathcal{F}_k(\mathbf{z}_m)$  is the  $k$  element of the Fourier transform of  $\mathbf{z}_m$ , where the  $l'', i$  element of  $\mathbf{z}_m$  is equal to  $x_{l'',i}^m c_{l'',i}$  for  $l'' = l$  and zero otherwise.

### A3 The reconstructed signal

To get the optimal reconstructed signal,  $\mathbf{s}$ , one should minimize the conditional probability distribution function  $\partial P(\mathbf{s}|\mathbf{y})/\partial \mathbf{s} = 0$ ,

$$\mathbf{s} = \mathbf{S}(\mathbf{S} + \mathbf{N})^{-1} \mathbf{y}, \quad (\text{A11})$$

or in Fourier-space,  $\partial P/\partial \mathcal{S} = 0$ ,

$$\mathcal{S}_k = \frac{\mathcal{P}_k}{\mathcal{P}_k + \sigma_N^2} \mathcal{Y}_k, \quad (\text{A12})$$

where  $\mathcal{S}_k$  is the  $k$  element of the Fourier transform of  $\mathbf{s}$ , and  $\mathcal{P}_k/(\mathcal{P}_k + \sigma_N^2)$  is the Wiener filter.